arXiv:2211.12786v1 [eess.IV] 23 Nov 2022

NONLINEAR EQUIVARIANT IMAGING: LEARNING MULTI-PARAMETRIC TISSUE MAPPING WITHOUT GROUND TRUTH FOR COMPRESSIVE QUANTITATIVE MRI

Ketan Fatania, Kwai Y. Chau, Carolin M. Pirkl, Marion I. Menzel, Peter Hall and Mohammad Golbabaee

ABSTRACT

Current state-of-the-art reconstruction for quantitative tissue maps from fast, compressive, Magnetic Resonance Fingerprinting (MRF), use supervised deep learning, with the drawback of requiring high-fidelity ground truth tissue map training data which is limited. This paper proposes NonLinear Equivariant Imaging (NLEI), a self-supervised learning approach to eliminate the need for ground truth for deep MRF image reconstruction. NLEI extends the recent Equivariant Imaging framework to nonlinear inverse problems such as MRF. Only fast, compressed-sampled MRF scans are used for training. NLEI learns tissue mapping using spatiotemporal priors: spatial priors are obtained from the invariance of MRF data to a group of geometric image transformations, while temporal priors are obtained from a nonlinear Bloch response model approximated by a pre-trained neural network. Tested retrospectively on two acquisition settings, we observe that NLEI (self-supervised learning) closely approaches the performance of supervised learning, despite not using ground truth during training.

Index Terms— Quantitative MRI, Magnetic Resonance Fingerprinting, Compressed Sensing, Inverse Problems, Self-Supervised Deep Learning, Equivariant Imaging

1. INTRODUCTION

Magnetic Resonance Fingerprinting (MRF) [1], is an accelerated Quantitative MRI (QMRI) method, for the acquisition of multi-parametric quantitative bio-property maps (QMaps) of the tissues, in a single time-efficient scan. The reduced acquisition times are due to aggressive spatiotemporal subsampling, which leads to aliasing artefacts in the MRF image time-series data, and as a result QMaps. Current state-of-the-art for MRF image reconstruction use supervised deep learning e.g. [2, 3, 4], for which training requires pairs of under-sampled, aliasing-contaminated MRF data, and their corresponding aliasing/artefact-free QMaps as ground truth. However, relying on ground truth is challenging, as: i) obtaining them requires long, clinically-infeasible scans, ii) long acquisitions are susceptible to motion artefacts (and correcting these may introduce interpolation artefacts), and iii) there is no real ground truth: each method for estimating ground truth QMaps comes with its own measurement effects and reconstruction artefacts, hence can only be considered a reference rather than real ground truth.

Therefore, an alternative approach to supervised learning which does not rely on ground truth during training, would be highly beneficial. This work proposes a self-supervised deep learning approach, NonLinear Equivariant Imaging (NLEI), to enable MRF quantitative mapping (reconstruction of QMaps), using only fast compressive MRF scans as training data, without requiring ground truth QMaps. We also apply linear Equivariant Imaging (EI) [5], the foundation for NLEI, for the first time to the MRF reconstruction problem. For competing algorithms, see [6, 7]. NLEI learns a reconstruction mapping for the MRF *nonlinear* inverse problem by incorporating spatiotemporal priors from the invariance of selected spatial transformations (e.g. rotations, flips) on estimated QMaps, and additionally (unlike EI) a differentiable model for the nonlinear Bloch response temporal dynamics approximated by a pre-trained neural network, BlochNet [8]. Tested retrospectively on two distinct MRF acquisitions, we observed that NLEI (self-supervised learning) closely approached the performance of supervised learning, despite not using ground truth during training.

KF, KYC, PH and MG are with the Department of Computer Science at the University of Bath, UK: (KF432@bath.ac.uk). CMP and MIM are with GE Healthcare, Germany. MIM is also with the Department of Physics at the Technical University of Munich, Germany and AImotion Bavaria at the Technische Hochschule Ingolstadt, Germany.

2. THE MRF INVERSE IMAGING PROBLEM

MRF adopts a spatiotemporal compressed sensing acquisition:

$$\boldsymbol{y} \approx \boldsymbol{A}\boldsymbol{x}(\boldsymbol{q}) \tag{1}$$

where $\boldsymbol{y} \in \mathbb{C}^{m\times T}$ are m k-space measurements taken at T timeframes, and $\boldsymbol{q} = \{\text{T1}, \text{T2}, \text{PD}\}$ are the unknown QMaps i.e. $n \times 3$ images of the tissues' T1 and T2 relaxation times and Proton Density (PD) across $n > m$ voxels. The linear acquisition operator $\boldsymbol{A} : \mathbb{C}^{n\times t} \to \mathbb{C}^{m\times T}$ models Fourier subsampling according to a set of temporally-varying k-space locations in each timeframe, combined with a temporal-domain SVD dimensionality reduction scheme [9, 3] i.e., $3 < t < T$. The Time-Series of Magnetisation Images (TSMI) for n voxels and t dimension-reduced timeframes are denoted by $\boldsymbol{x} \in \mathbb{C}^{n\times t}$. The TSMIs' magnetisation responses (fingerprints) per voxel v, are *nonlinearly* related to the tissue properties T1 and T2 relaxation times by the solutions of the Bloch differential equations, $\mathcal{B}$, scaled by the Proton Density, PD [1, 10]:

$$\boldsymbol{x}_v \approx \text{PD}_v\, \mathcal{B}(\text{T1}_v, \text{T2}_v) \tag{2}$$

The compressive nature of the acquisitions makes the estimation of QMaps ($\boldsymbol{q}$) from the undersampled MRF measurements ($\boldsymbol{y}$) a nonlinear ill-posed inverse problem (1).

The Bloch model can temporally constrain (1), but alone is absent of spatially-constraining priors to make the inverse problem well-posed. While supervised deep image reconstruction models can learn effective spatial priors from ground truth QMaps, i.e. interdependencies across image voxels, they would impose a significant scan-time challenge, as mentioned. We therefore build on the EI self-supervised learning framework to obtain a set of more generic (but still effective) spatially-constraining image priors, with the advantage of using only fast compressed MRF scans as training data.

3. EQUIVARIANT IMAGING

Equivariant Imaging [5] exploits the assumption that an image (to be reconstructed) is invariant to certain types of transformations, e.g. reflections and rotations, in order to train a deep image reconstruction model ($\boldsymbol{f}$) in a self-supervised fashion. This is done by applying

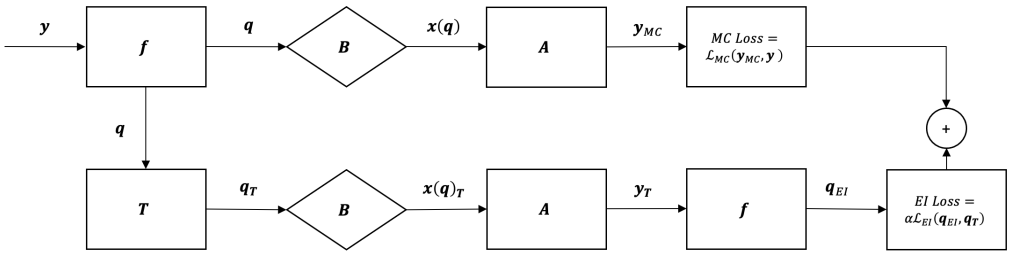


Fig. 1: Our NLEI algorithm for self-supervised learning of MRF quantitative mapping. See Non-Linear Equivariant Imaging for details.

the acquisition operator $\boldsymbol{A}$, on the reconstructed transformed images obtained from $\boldsymbol{f}$, to yield new observations (k-space measurements) with information outside the range of the original observations. The new observations, once reconstructed by the same model $\boldsymbol{f}$, must result in a transformed image compared to the original reconstruction.

While the original EI idea [5] works for linear inverse problems, i.e. estimating TSMIs ($\boldsymbol{x}$) and not QMaps ($\boldsymbol{q}$) in (1), it can be suboptimal for MRF by neglecting temporally-constraining Bloch response priors that nonlinearly relate the TSMIs to lower-dimensional QMaps. Our NLEI algorithm builds on EI to additionally incorporate the Bloch priors (2) to estimate the QMaps in the nonlinear problem (1). Fig.1 shows the NLEI training pipeline.

Non-Linear Equivariant Imaging: The reconstruction model $\boldsymbol{f}(\boldsymbol{y}) : \boldsymbol{A}^H\boldsymbol{y} \rightarrow \boldsymbol{q}$ is a U-Net CNN following [5], which learns a spatiotemporal mapping from aliased TSMIs, obtained from back-projected k-space measurements ($\boldsymbol{A}^H\boldsymbol{y}$), to the artefact-free QMaps. $\boldsymbol{A}^H$ is the adjoint of $\boldsymbol{A}$, and our experiments used the temporal dimension $t = 10$ for the complex-valued TSMIs, leading to 20ch stacked real and imaginary parts for the inputs of $\boldsymbol{f}$, whereas outputs are 4ch QMaps of T1, T2, PD_{real} and PD_{imag}. Training uses a weighted sum of two MSE losses $\mathcal{L}_{MC} + \alpha\mathcal{L}_{EI}$ ($\alpha > 0$).

- **Measurement Consistency (MC) loss, $\mathcal{L}_{MC}(\boldsymbol{y}_{MC}, \boldsymbol{y})$:** is a routinely-used loss in compressed sensing literature, first applied to deep MRF in [8] for minimising discrepancies between scanner k-space measurements $\boldsymbol{y}$, and those obtained from the reconstructed QMaps $\boldsymbol{q} := \boldsymbol{f}(\boldsymbol{y})$, following the nonlinear forward model (1). To be specific, a pre-trained BlochNet model ($\boldsymbol{B}$) which approximates (2) was used to map $\boldsymbol{q}$ to TSMIs $\boldsymbol{x}(\boldsymbol{q}) \approx \boldsymbol{B}(\boldsymbol{q})$ with PD_{real} and PD_{imag} used to obtain complex-valued TSMIs, followed then by the compressed subsampling operator $\boldsymbol{A}$, to obtain k-space data $\boldsymbol{y}_{MC} := \boldsymbol{A} \circ \boldsymbol{B}(\boldsymbol{q})$. Minimising $\mathcal{L}_{MC}$ enables $\boldsymbol{f}$ to find an inverse mapping for $\boldsymbol{A} \circ \boldsymbol{B}$, where the reconstructed QMaps respect the forward model physics.
- **EI loss $\mathcal{L}_{EI}(\boldsymbol{q}_{EI}, \boldsymbol{q}_{\boldsymbol{T}})$:** minimises discrepancies between reconstructed $\boldsymbol{q}$, and the spatially-transformed reconstructed QMaps $\boldsymbol{q}_{EI}$, (Fig.1). To be specific, spatial transformations $\boldsymbol{T}$, are applied to the QMaps $\boldsymbol{q} := \boldsymbol{f}(\boldsymbol{y})$, reconstructed from the original (scanner) k-space data. An approximate $\boldsymbol{A} \circ \boldsymbol{B}$ of the nonlinear forward model (1) are applied to $\boldsymbol{q}_{\boldsymbol{T}} := \boldsymbol{T}(\boldsymbol{q})$, to obtain new k-space measurements, which were then reconstructed by $\boldsymbol{f}$ into $\boldsymbol{q}_{EI} := \boldsymbol{f} \circ \boldsymbol{A} \circ \boldsymbol{B} \circ \boldsymbol{T}(\boldsymbol{q})$. The EI loss enables $\boldsymbol{f}$ to learn a reconstruction mapping in a self-supervised manner that respects the image invariance properties, i.e. $\boldsymbol{f}$ should learn that $\boldsymbol{q}$ and $\boldsymbol{q}_{EI}$ are only different by a transformation: $\boldsymbol{T}(\boldsymbol{q}) \approx \boldsymbol{q}_{EI}$.

Linear Equivariant Imaging: The linear EI algorithm [5] for MRF can be reduced from the NLEI pipeline in Fig.1: (i) let $\boldsymbol{f}(\boldsymbol{y}) : \boldsymbol{A}^H\boldsymbol{y} \rightarrow \boldsymbol{x}$ reconstruct a TSMI, and (ii) remove the BlochNet $\boldsymbol{B}$ (diamond-shapes in Fig.1) responsible for the forward model's nonlinearity. The result is the EI algorithm to reconstruct an artefact-reduced TSMI $\boldsymbol{x}$, albeit uninformed/unconstrained by the Bloch response priors. An MRF dictionary-matching step [1] then can be used to estimate QMaps from the EI-reconstructed TSMI.

BlochNet, $\boldsymbol{B}$ [8]**:** approximates (2) by a differentiable neural network model, that is kept frozen and used within the NLEI's training pipeline (Fig.1) to add temporal Bloch response priors. Implemented by a CNN of 2 hidden layers (each with 300 filters, ReLU activations), BlochNet uses 1×1 filters to process QMaps (input) in a voxel-wise manner and output the corresponding TSMI i.e. $\boldsymbol{x}(q) \approx \boldsymbol{B}(\boldsymbol{q})$. This network is trained offline from NLEI. Training data uses an SVD dimension-reduced ($t = 10$) FISP-MRF dictionary [9] with 94,777 fingerprints, that are simulated Bloch responses (using EPG simulator [11]) for combinations of T1/T2 values in a logarithmically-sampled grid $(\text{T1}, \text{T2}) \in [0.01, 6] \times [0.004, 4]$ (sec).

Transformations, $\boldsymbol{T}$: An important component of EI is the selection of appropriate transformations to learn image invariances. For compressed sensing MRI, randomly selected rotations have been successfully used by EI [7], while shift transformations have no benefit for Fourier based acquisitions [5]. For our work, the NLEI and EI use a random selection from 7 transformations defined by combinations of 90° rotations and vertical flips, accounting for all orientations: 1) Vertical Flip, 2) 90° Rotation, 3) Vertical Flip with 90° Rotation, 4) 180° Rotation, 5) Vertical Flip with 180° Rotation, 6) 270° Rotation and 7) Vertical Flip with 270° Rotation. We limit rotation angles to multiples of 90° to prevent interpolation artefacts.

4. NUMERICAL EXPERIMENTS

Dataset: We used a dataset of T1, T2 and PD QMaps of 2D axial brain scans from 8 subjects across 15 slices. Complex-valued TSMIs and k-space MRF data were retrospectively simulated from these QMaps via (2) and (1), correspondingly. The reference QMaps and TSMIs had spatial dimensions of $n = 224 \times 224$ pixels with head-masks applied, which were generated using the Proton Density. For the Bloch response model a truncated FISP-MRF protocol [10] was used with $T = 200$ repetitions i.e. 5 times less (accelerated) than the original FISP-MRF. For MRF k-space data, we simulated single-coil acquisitions using two distinct cartesian (FFT) k-space subsampling patterns evolving across each temporal frame: (i) a rotating Spiral, as in [8] and (ii) shifting horizontal lines using multi-shot Echo Planar Imaging (EPI) [12]. We sampled $m = 771$ k-space locations in each timeframe, corresponding to a spatial compression ratio of 65:1. The TSMIs were dimension-reduced ($t = 10$) following [9]. The dataset was split into 105 slices from 7 subjects for training, and 15 slices from the 8^{th} subject for testing.

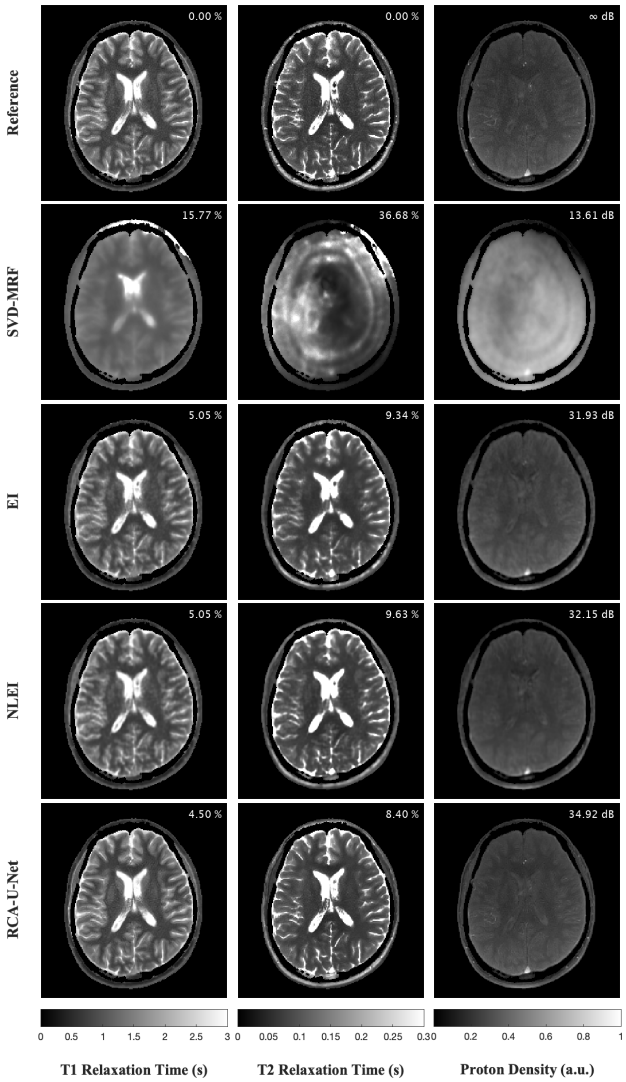


Fig. 2: Tissue Map Results using Spiral Subsampling for Slice 10 of 15, with MAPE (%) for T1 and T2, and PSNR (dB) for PD.

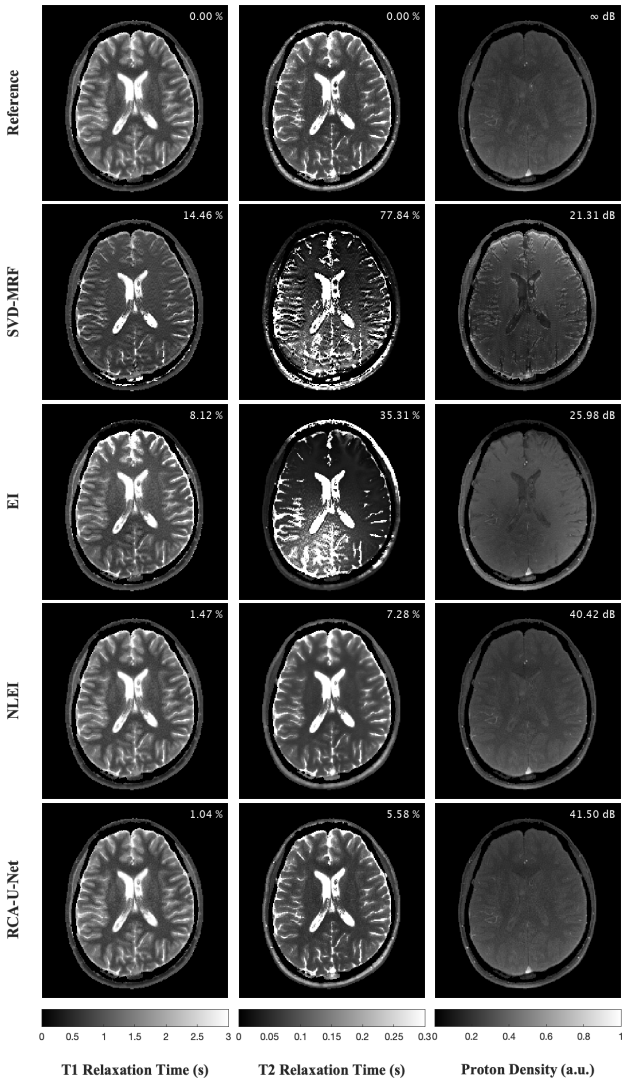


Fig. 3: Tissue Map Results using EPI Subsampling for Slice 10 of 15, with MAPE (%) for T1 and T2, and PSNR (dB) for PD.

Tested Algorithms: We compared the performance of the proposed NLEI to EI [5], SVD-MRF [9] and RCA-U-Net [2] baselines. SVD-MRF is a non-data driven approach which reconstructs backprojected (aliased) TSMI $\boldsymbol{A}^H\boldsymbol{y}$ from k-space data, followed by MRF dictionary-matching to estimate QMaps. Other tested algorithms use deep learning to further process the backprojected TSMIs to produce aliasing-reduced estimations. RCA-U-Net is a state-of-the-art deep supervised learning MRF model that uses ground truth QMaps for training. Separate RCA-U-Net models were trained for T1, T2, PD_{real} and PD_{imag} following [2] using 1000 epochs, L1 loss, and linearly decaying learning rate from 200 to 1000 epochs. On the other hand, NLEI and EI are self-supervised learning models that do not use ground truth for training (they only use under-sampled MRF k-space data). NLEI and EI used the U-Net as in [5], without the residual connection between the initial and final layers, and trained using 1000 epochs, batch size 2, Adam optimiser, weight decay 10^{-8}, initial learning rate 5×10^{-4} decreasing by factor 10 at 300 epochs. We used 3 randomly selected transformations per iteration from the 7 previously defined, and applied them across each batch to create new batch sizes of 6. Optimal values for α were found experimentally: 10^{-8} for NLEI Spiral, 10^{-4} for NLEI EPI, 10^{-5} for EI Spiral, and 10^{-2} for EI EPI.

Evaluation Metrics: We used the Mean Absolute Error (MAE), Mean Absolute Percentage Error (MAPE), Peak Signal-to-Noise-Ratio (PSNR) and Structural Similarity Index Measure (SSIM). Head-masks were applied to all reconstructions and metrics were then calculated and averaged across 15 test slices.

Results and Discussion: Metrics in Table 1, for both subsampling patterns, show a clear progression in performance from SVD-MRF to EI, NLEI and RCA-U-Net, with NLEI (self-supervised approach trained without ground truth) approaching the performance of the supervised model RCA-U-Net. The results in Fig.2 show similar performance for NLEI and EI, while Fig.3 shows NLEI outperforms SVD-MRF and EI, while being close to RCA-U-Net. SVD-MRF, NLEI and EI exhibit blurring, which can also be seen in RCA-U-Net to a lesser extent. This is intrinsic to spiral subsampling due to prioritised sampling of low frequencies at the centre of k-space.

		Spiral				EPI			
		SVD-MRF	EI	NLEI	RCA-U-Net	SVD-MRF	EI	NLEI	RCA-U-Net
MAE (s)	T1	0.1371	0.0577	0.0532	0.0473	0.1658	0.1096	0.0180	0.0121
	T2	0.0484	0.0178	0.0162	0.0134	0.1004	0.0451	0.0139	0.0094
MAPE (%)	T1	12.2519	5.0527	4.2236	3.8465	13.5611	7.4711	1.2951	0.9502
	T2	34.9255	9.3400	8.6272	7.3329	68.3580	33.5549	6.7534	5.2095
PSNR (dB)	TSMI	11.3135	26.0396	-	-	17.1590	3.2324	-	-
	T1	23.9384	33.2161	33.6557	34.7350	22.4085	23.3885	39.2725	42.9782
	T2	25.7089	34.8714	36.7658	38.3916	20.6887	31.1333	37.0679	41.1515
	PD	13.9547	31.9296	31.4679	34.0273	21.5492	25.9406	38.2944	39.7831
SSIM	TSMI	0.5979	0.7721	-	-	0.5819	0.5542	-	-
	T1	0.8195	0.9409	0.9425	0.9558	0.8962	0.9230	0.9898	0.9967
	T2	0.8469	0.9514	0.9537	0.9688	0.7529	0.8376	0.9642	0.9838
	PD	0.7676	0.8896	0.8913	0.9224	0.7659	0.9050	0.9837	0.9906

Table 1: Evaluation metrics, averaged over 15 test slices, show increasing performance for each acquisition scheme, moving from SVD-MRF [9], EI [5], NLEI (ours) to RCA-U-Net [2]. NLEI (self-supervised learning) performs closest to RCA-U-Net (supervised learning).

We acknowledge that no noise was used in our study, which is intrinsic to the MRF process. Robust Equivariant Imaging (REI) [7] has recently been proposed which directly addresses noise within scans. We hope to extend our work to REI to address this drawback.

NLEI succeeds over EI by addressing the nonlinearity of the MRF inverse problem which exploits additional temporal-domain priors, while EI only takes advantage of the spatial-domain image priors obtained form transformation invariances. Supervised learning (RCA-U-Net) provides the best performance, with self-supervised learning (NLEI) closely approaching. The advantages of using only fast MRF scans for training, no ground truth requirement, and flexibility across pathologies which may not be available in the ground truth, may make NLEI a competitive alternative.

5. CONCLUSION

A proof-of-concept for a self-supervised learning approach (NLEI) for MRF multi-parametric quantitative tissue mapping was proposed. The method was validated on two cartesian (FFT) k-space sampling patterns on retrospectively simulated MRF data. The NLEI's performance was observed to approach the state-of-the-art supervised learning methods, despite not using ground truth for training. Future work will include extensions to address noisy, non-cartesian acquisitions from prospective in-vivo scans.

6. COMPLIANCE WITH ETHICAL STANDARDS

This research study was conducted retrospectively using anonymised human subject scans made available by GE Healthcare who obtained informed consent in compliance with the German Act on Medical Devices. Approval was granted by the Ethics Committee of The University of Bath (Date. Sept 2021 / No. 6568).

7. ACKNOWLEDGMENTS

CMP and MIM are supported by the EU's Horizon 2020 (grant No. 952172). MG is supported by the EPSRC grant EP/X001091/1.

8. REFERENCES

[1] D. Ma et al., "Magnetic resonance fingerprinting," *Nature*, vol. 495, no. 7440, pp. 187–192, 2013.

[2] Z. Fang et al., "Rca-u-net: Residual channel attention u-net for fast tissue quantification in magnetic resonance fingerprinting," in *MICCAI*, 2019, pp. 101–109.

[3] M. Golbabaee et al., "Compressive mri quantification using convex spatiotemporal priors and deep encoder-decoder networks," *Medical Image Analysis*, vol. 69, pp. 101945, 2021.

[4] K. Fatania, C. M. Pirkl, M. I. Menzel, P. Hall, and M. Golbabaee, "A plug-and-play approach to multiparametric quantitative mri: Image reconstruction using pre-trained deep denoisers," in *2022 IEEE 19th International Symposium on Biomedical Imaging (ISBI)*, 2022, pp. 1–4.

[5] D. Chen, J. Tachella, and M. E. Davies, "Equivariant imaging: Learning beyond the range space," in *2021 IEEE/CVF Intl. Conf. on Computer Vision (ICCV)*, Oct 2021, pp. 4359–4368.

[6] M. Gao, H. Ye, T. H. Kim, Z. Zhang, S. So, and B. Bilgic, "Accurate parameter estimation using scan-specific unsupervised deep learning for relaxometry and mr fingerprinting," 2021.

[7] D. Chen, J. Tachella, and M. E. Davies, "Robust equivariant imaging: a fully unsupervised framework for learning to image from noisy and partial measurements," in *2022 IEEE/CVF Conference on Computer Vision and Pattern Recognition (CVPR)*, June 2022, pp. 5637–5646.

[8] D. Chen, M. E. Davies, and M. Golbabaee, "Compressive mr fingerprinting reconstruction with neural proximal gradient iterations," in *MICCAI*, 2020, pp. 13–22.

[9] D. F. McGivney et al., "Svd compression for magnetic resonance fingerprinting in the time domain," *IEEE Trans. Med. Imag.*, vol. 33, no. 12, pp. 2311–2322, 2014.

[10] Y. Jiang, D. Ma, N. Seiberlich, V. Gulani, and M. A. Griswold, "Mr fingerprinting using fast imaging with steady state precession (fisp) with spiral readout," *Magnetic Resonance in Medicine*, vol. 74, no. 6, pp. 1621–1631, 2015.

[11] M. Weigel, "Extended phase graphs: dephasing, rf pulses, and echoes-pure and simple," *Journal of Magnetic Resonance Imaging*, vol. 41, no. 2, pp. 266–295, 2015.

[12] A. J. V. Benjamin et al., "Multi-shot echo planar imaging for accelerated cartesian mr fingerprinting: an alternative to conventional spiral mr fingerprinting," *Magnetic Resonance Imaging*, vol. 61, pp. 20–32, 2019.

arXiv:2211.12786v1 [eess.IV] 23 Nov 2022

SUPPLEMENTARY MATERIAL: NONLINEAR EQUIVARIANT IMAGING: LEARNING MULTI-PARAMETRIC TISSUE MAPPING WITHOUT GROUND TRUTH FOR COMPRESSIVE QUANTITATIVE MRI

1. DATA ACQUIRED

Data was obtained from a 3T GE scanner (MR750w system - GE Healthcare, Waukesha, WI) with 8-channel receive-only head RF coil, 230×230 mm^2 FOV, 5 mm slice thickness, and used a FISP-MRF acquisition protocol with $T = 1000$ repetitions, same flip angles as [1], inversion time 18 ms, repetition time 10 ms and echo time 1.8 ms. QMaps were reconstructed using the LRTV algorithm [2] with regularisation parameter $\lambda = 0$. The ground truth (reference) and simulated MRF datasets were then generated as described in the main paper.

2. EVALUATION METRICS - EXTENDED

For QMaps, the Mean Absolute Error (MAE), Mean Absolute Percentage Error (MAPE), Peak Signal-to-Noise-Ratio (PSNR) and Structural Similarity Index Measure (SSIM) were used. The magnitude of $\text{PD}_{\text{complex}}$ normalised between 0 and 1 was used for evaluation. For TSMIs, the PSNR and SSIM were used. The data ranges used for PSNR and SSIM were 6s for T1, 4s for T2, 1 for PD, and the arithmetic range of each TSMI. Head-masks were applied on all reconstructions and the metrics were then calculated and averaged across 15 test slices.

3. SEARCHING FOR OPTIMAL VALUES OF α

We performed a number of experiments to determine the optimal values of the regularisation constant for the Equivariance Imaging (EI) loss, α, for Non-Linear Equivariant Imaging (NLEI) and linear Equivariant Imaging (EI). The same methodology was used for both NLEI and EI, as described in the main paper. The performance of NLEI and EI was tested with Spiral and EPI subsampling patterns using α values of 0, Measurement Consistency (MC) only, and $10^{\{-12,-11,-10,-9,-8,-7,-6,-5,-4,-3,-2,-1,0,1,2,3,4,5,6\}}$. The results presented in Section. 3.1 are averaged over 15 test slices. The results presented in Section. 3.2 are the results presented in Section. 3.1 averaged using all QMaps, T1, T2 and PD. All results were masked using a head mask as mentioned in the main paper.

3.1. Results Grouped by Metric

We initially group the Time-Series Magnetisation Images (TSMIs) and Quantitative Maps (QMaps) (T1, T2 and Proton Density, PD) results by metric. We find a range of values for α which give the best performance with respect to particular metrics and QMaps, see Tables 1 to 8 and Figures 1 to 8 for NLEI, and Tables 9 to 16 and Figures 9 to 16 for EI.

3.2. Optimal α Selection

To determine the optimal value of α, the mean of all QMap results for each metric, for each value of α is taken, e.g for $\alpha = 0$ and NLEI with Spiral subsampling, the mean is taken using the MAE results for T1, T2 and PD, then the mean is taken using the MAPE results for T1, T2 and PD, and similarly for PSNR and SSIM. We then determined the best averaged QMaps value of each metric against α, see Tables 17 to 20. The optimal value of α was then chosen according to two criteria: (i) the number of metrics which agree to a particular value of α and (ii) according to metric importance given by the order 1) MAPE, 2) MAE, 3) PSNR and 4) SSIM. We prioritise data quality metrics, MAPE and MAE, over image quality metrics, PSNR and SSIM.

We find the optimal value of α is dependent on the algorithm used, NLEI or EI, and the subsampling pattern used, Spiral or EPI, see Tables 17 to 20.

4. REFERENCES

[1] Y. Jiang, D. Ma, N. Seiberlich, V. Gulani, and M. A. Griswold, "Mr fingerprinting using fast imaging with steady state precession (fisp) with spiral readout," *Magnetic Resonance in Medicine*, vol. 74, no. 6, pp. 1621–1631, 2015.

[2] M. Golbabaee et al., "Compressive mri quantification using convex spatiotemporal priors and deep encoder-decoder networks," *Medical Image Analysis*, vol. 69, pp. 101945, 2021.

NLEI with Spiral Subsampling - Mean MAE			
α	T1 MAE (s)	T2 MAE (s)	PD (a.u)
0	0.0538	0.0164	0.0147
10^{-12}	0.0521	0.0159	0.0166
10^{-11}	0.0535	0.0161	0.0162
10^{-10}	0.0545	0.0163	0.0163
10^{-9}	0.0523	0.0159	0.0174
10^{-8}	0.0563	0.0178	0.0229
10^{-7}	0.0540	0.0167	0.0177
10^{-6}	0.0533	0.0163	0.0153
10^{-5}	0.0506	0.0157	0.0135
10^{-4}	0.0525	0.0163	0.0171
10^{-3}	0.0518	0.0158	0.0146
10^{-2}	0.0530	0.0164	0.0153
10^{-1}	0.0543	0.0165	0.0223
1	0.0601	0.0192	0.0231
10^{1}	0.0734	0.0209	0.0499
10^{2}	0.1451	0.0315	0.1849
10^{3}	0.1767	0.0315	0.1737
10^{4}	0.1777	0.0310	0.1050
10^{5}	0.1798	0.0305	0.2523
10^{6}	0.1799	0.0305	0.2931

Table 1: The average MAE across 15 test slices for each QMap, T1, T2 and PD, against the Equivariant loss hyperparameter, α, for NonLinear Equivariant Imaging (NLEI) with Spiral Subsampling.

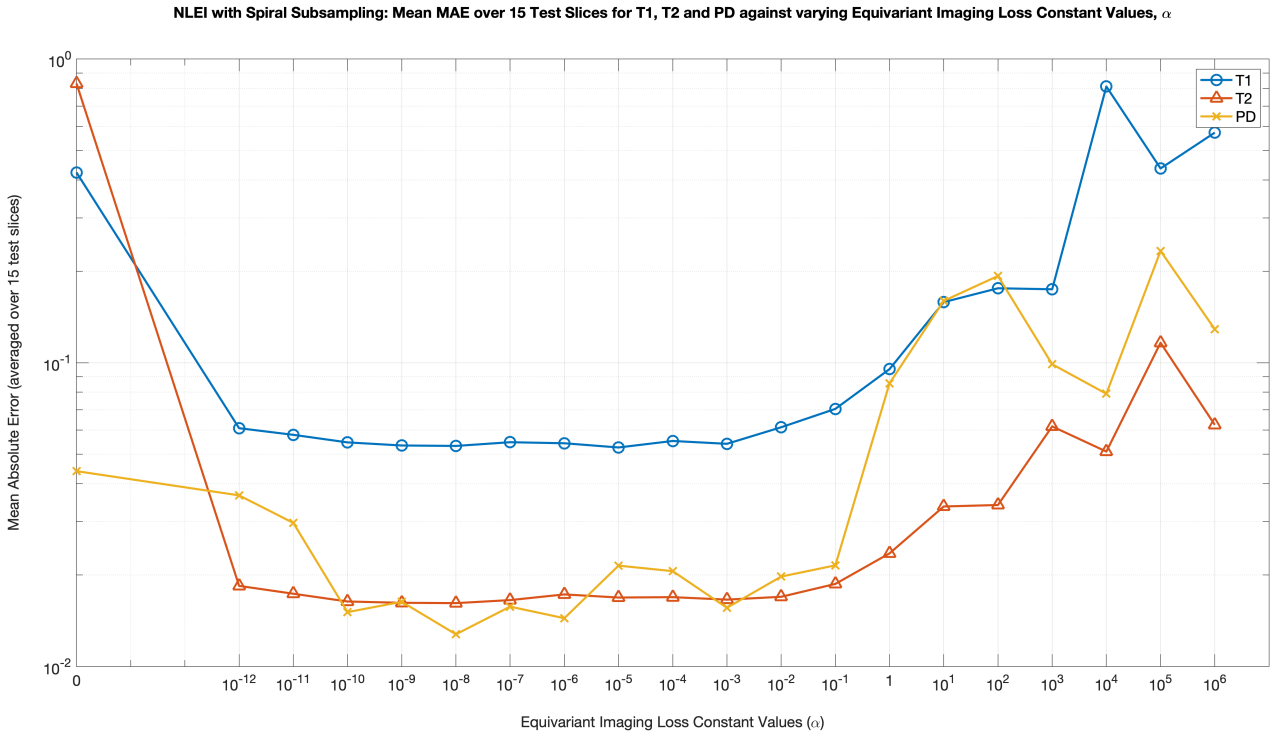


Fig. 1: The graph for the average MAE across 15 test slices for each QMap, T1, T2 and PD, against the Equivariant loss hyperparameter, α, for NonLinear Equivariant Imaging (NLEI) with Spiral Subsampling.

NLEI with Spiral Subsampling - Mean MAPE			
α	T1 MAPE (%)	T2 MAPE (%)	PD MAPE (%)
0	49.0090	1149.3624	16.0226
10^{-12}	4.7014	9.9862	14.0194
10^{-11}	4.4575	9.9056	11.4266
10^{-10}	4.2462	8.7898	5.7634
10^{-9}	4.2033	8.7624	6.2499
10^{-8}	4.2236	8.6272	4.8952
10^{-7}	4.3001	8.7374	6.1698
10^{-6}	4.2363	9.7763	5.6213
10^{-5}	4.1260	9.8378	8.1353
10^{-4}	4.2679	9.1630	8.0242
10^{-3}	4.1794	9.0589	5.9696
10^{-2}	4.5183	9.1437	7.7790
10^{-1}	5.1712	10.4649	8.3138
1	6.9669	14.0936	32.4467
10^{1}	12.2393	22.5962	62.7768
10^{2}	14.1843	23.3730	75.4141
10^{3}	13.8452	60.0660	36.9571
10^{4}	67.4086	29.5688	29.7432
10^{5}	32.6355	93.1951	95.7941
10^{6}	45.2356	40.6930	53.8938

Table 2: The average MAPE across 15 test slices for each QMap, T1, T2 and PD, against the Equivariant loss hyperparameter, α, for NonLinear Equivariant Imaging (NLEI) with Spiral Subsampling.

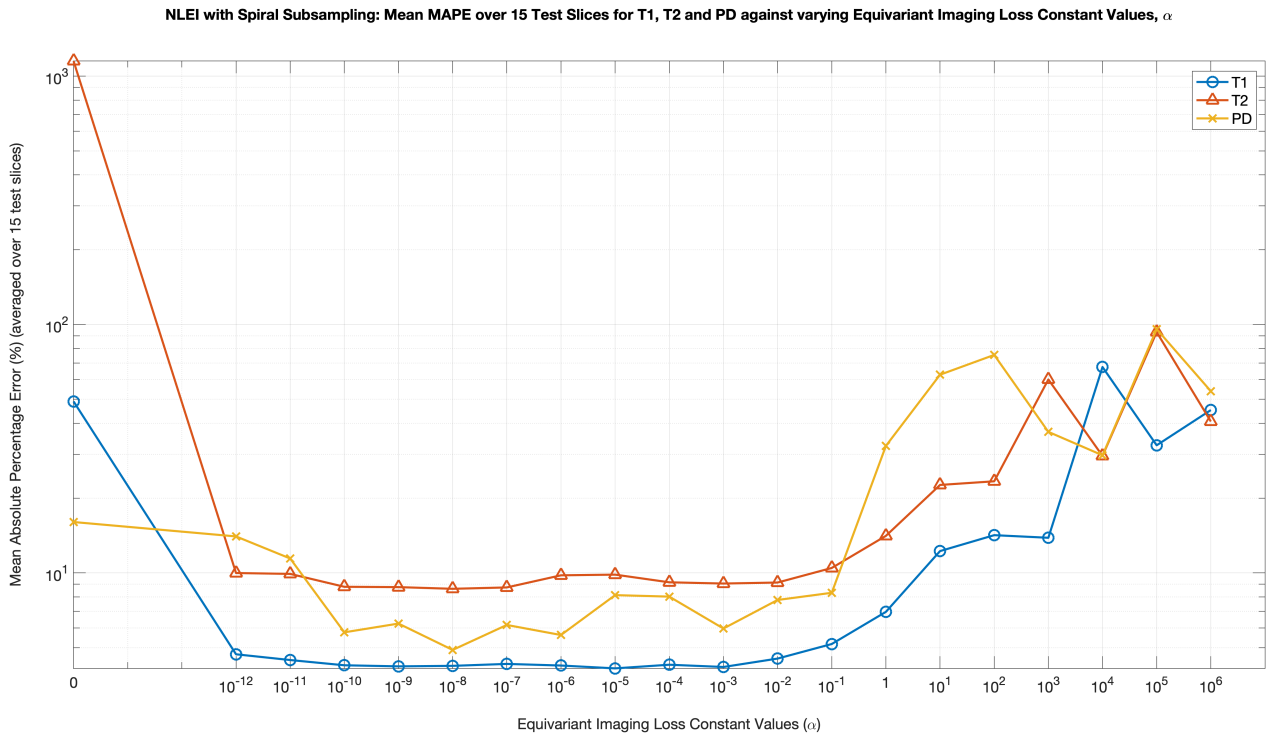


Fig. 2: The graph for the average MAPE across 15 test slices for each QMap, T1, T2 and PD, against the Equivariant loss hyperparameter, α, for NonLinear Equivariant Imaging (NLEI) with Spiral Subsampling.

NLEI with Spiral Subsampling - Mean PSNR			
α	T1 PSNR (dB)	T2 PSNR (dB)	PD PSNR (dB)
0	10.9272	3.5530	22.7114
10^{-12}	32.4374	35.7135	24.0572
10^{-11}	32.8425	36.2210	25.7408
10^{-10}	33.3695	36.8044	30.6028
10^{-9}	33.5523	36.7713	30.2546
10^{-8}	33.6557	36.7658	31.4679
10^{-7}	33.3289	36.5065	30.2682
10^{-6}	33.3965	35.1671	30.7866
10^{-5}	33.6677	35.8088	28.2647
10^{-4}	33.2579	36.3769	28.4831
10^{-3}	33.3009	36.7610	30.3547
10^{-2}	31.9512	36.4093	28.8938
10^{-1}	30.8338	35.8817	28.0999
1	28.4101	34.4717	16.9311
10^{1}	24.6209	31.9920	11.5577
10^{2}	23.8994	32.0548	9.4567
10^{3}	23.8594	30.4008	13.2923
10^{4}	13.1451	29.9750	16.8556
10^{5}	17.7444	25.6197	9.4317
10^{6}	15.8294	29.1467	13.4438

Table 3: The average PSNR across 15 test slices for each QMap, T1, T2 and PD, against the Equivariant loss hyperparameter, α, for NonLinear Equivariant Imaging (NLEI) with Spiral Subsampling.

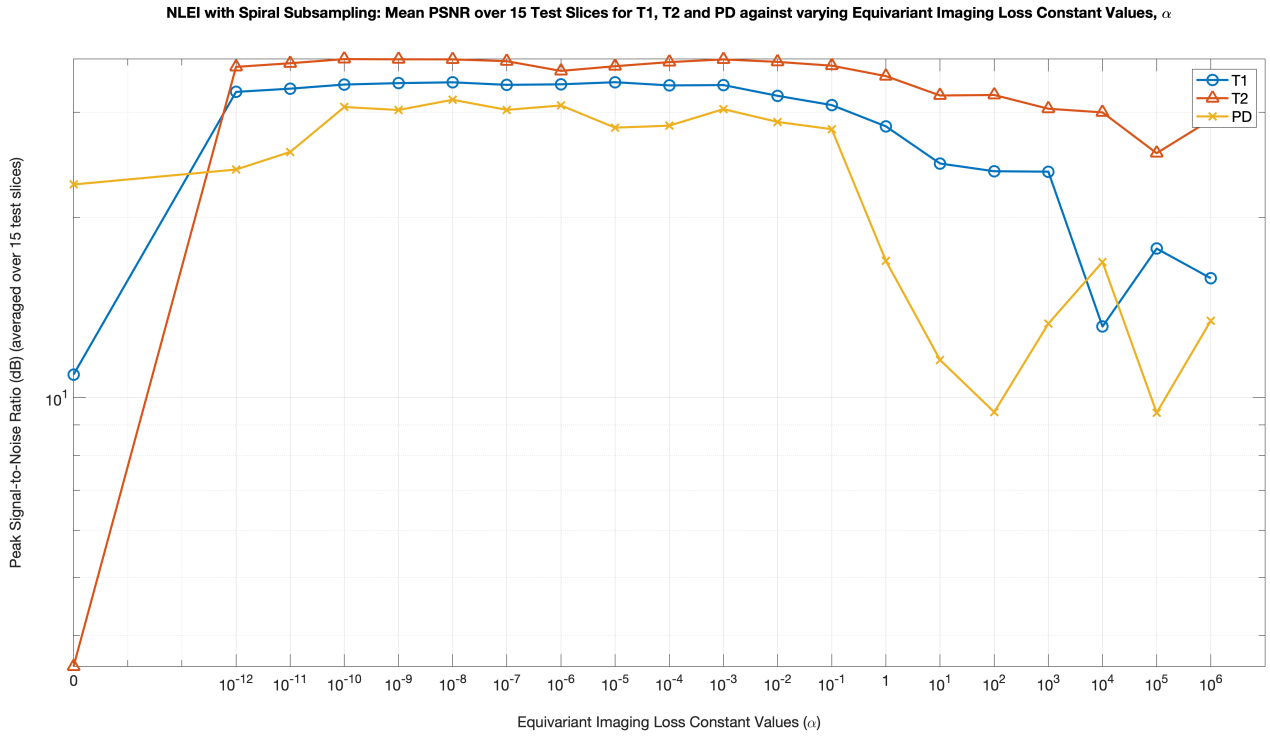


Fig. 3: The graph for the average PSNR across 15 test slices for each QMap, T1, T2 and PD, against the Equivariant loss hyperparameter, α, for NonLinear Equivariant Imaging (NLEI) with Spiral Subsampling.

NLEI with Spiral Subsampling - Mean SSIM			
α	T1 SSIM	T2 SSIM	PD SSIM
0	0.9170	0.9275	0.8114
10^{-12}	0.9287	0.9422	0.8589
10^{-11}	0.9347	0.9485	0.8672
10^{-10}	0.9402	0.9530	0.8891
10^{-9}	0.9414	0.9532	0.8901
10^{-8}	0.9425	0.9537	0.8913
10^{-7}	0.9394	0.9513	0.8873
10^{-6}	0.9400	0.9509	0.8872
10^{-5}	0.9433	0.9534	0.8846
10^{-4}	0.9389	0.9510	0.8798
10^{-3}	0.9393	0.9529	0.8862
10^{-2}	0.9248	0.9510	0.8803
10^{-1}	0.9044	0.9440	0.8655
1	0.8512	0.9196	0.8021
10^{1}	0.7764	0.8745	0.7328
10^{2}	0.7661	0.8787	0.7033
10^{3}	0.7671	0.8068	0.7761
10^{4}	0.4510	0.7478	0.6608
10^{5}	0.5970	0.2888	0.6467
10^{6}	0.4746	0.6062	0.6894

Table 4: The average SSIM across 15 test slices for each QMap, T1, T2 and PD, against the Equivariant loss hyperparameter, α, for NonLinear Equivariant Imaging (NLEI) with Spiral Subsampling.

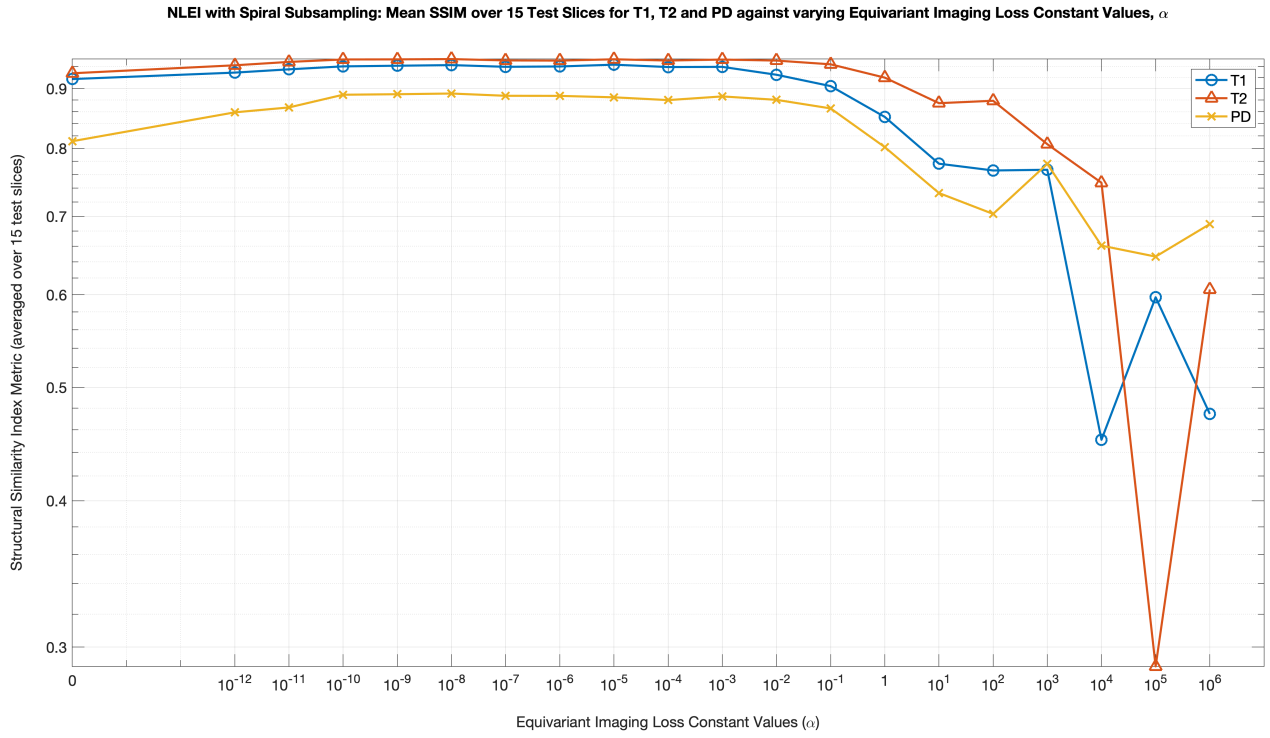


Fig. 4: The graph for the average SSIM across 15 test slices for each QMap, T1, T2 and PD, against the Equivariant loss hyperparameter, α, for NonLinear Equivariant Imaging (NLEI) with Spiral Subsampling.

NLEI with EPI Subsampling - Mean MAE			
α	T1 MAE (s)	T2 MAE (s)	PD (a.u)
0	0.0308	0.0176	0.0084
10^{-12}	0.0207	0.0139	0.0063
10^{-11}	0.0212	0.0155	0.0069
10^{-10}	0.0209	0.0159	0.0067
10^{-9}	0.0192	0.0140	0.0065
10^{-8}	0.0241	0.0162	0.0083
10^{-7}	0.0194	0.0139	0.0060
10^{-6}	0.0220	0.0145	0.0063
10^{-5}	0.0224	0.0158	0.0066
10^{-4}	0.0180	0.0139	0.0063
10^{-3}	0.0185	0.0135	0.0065
10^{-2}	0.0223	0.0167	0.0078
10^{-1}	0.0517	0.0203	0.0159
1	0.2465	0.0569	0.1832
10^{1}	0.3509	0.0539	0.0716
10^{2}	0.4396	0.0494	0.0588
10^{3}	0.9787	0.2618	0.0594
10^{4}	0.5131	0.0663	0.2968
10^{5}	0.5092	0.0505	0.2831
10^{6}	0.5667	0.0393	0.2615

Table 5: The average MAE across 15 test slices for each QMap, T1, T2 and PD, against the Equivariant loss hyperparameter, α, for NonLinear Equivariant Imaging (NLEI) with EPI Subsampling.

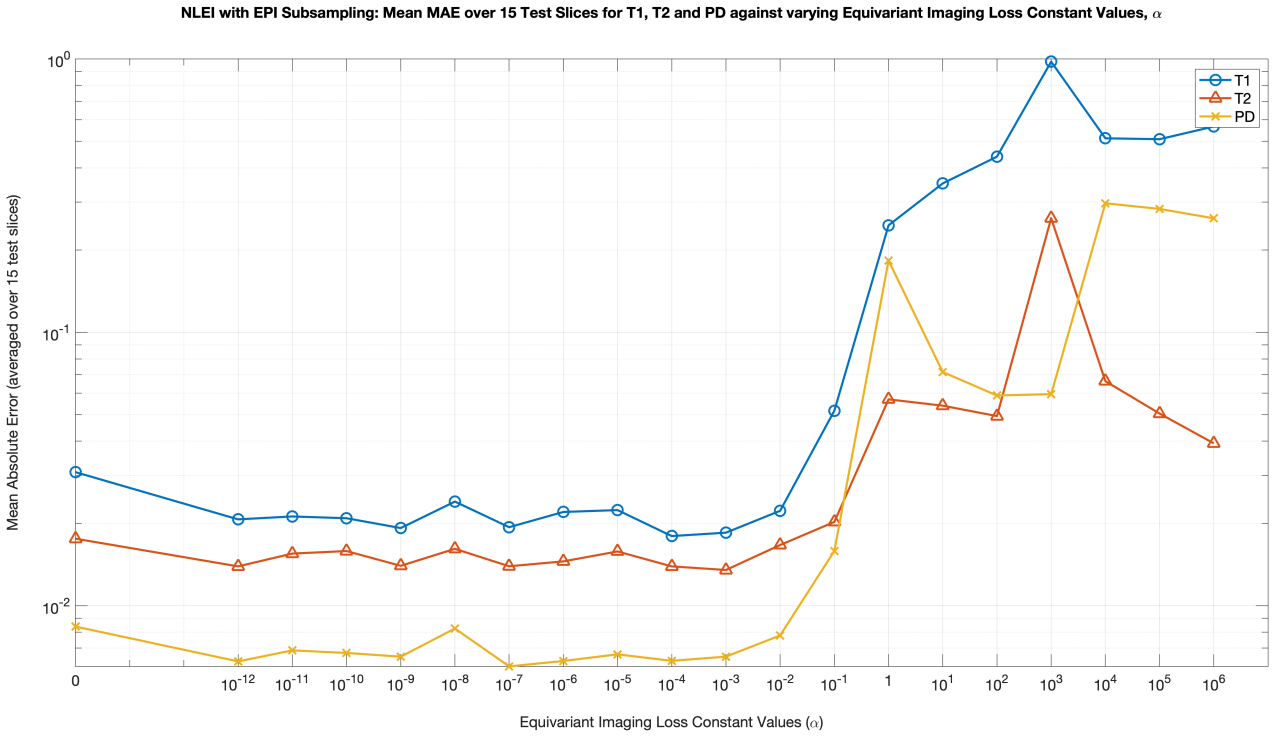


Fig. 5: The graph for the average MAE across 15 test slices for each QMap, T1, T2 and PD, against the Equivariant loss hyperparameter, α, for NonLinear Equivariant Imaging (NLEI) with EPI Subsampling.

NLEI with EPI Subsampling - Mean MAPE			
α	T1 MAPE (%)	T2 MAPE (%)	MAPE (%)
0	2.3088	8.3396	3.1016
10^{-12}	1.5280	6.6779	2.2962
10^{-11}	1.5429	7.3496	2.5243
10^{-10}	1.5104	7.2350	2.4924
10^{-9}	1.4179	7.0652	2.3705
10^{-8}	1.8458	8.0811	2.9816
10^{-7}	1.4208	6.8627	2.1973
10^{-6}	1.5034	7.1576	2.3248
10^{-5}	1.5572	7.8345	2.5453
10^{-4}	1.2951	6.7534	2.3250
10^{-3}	1.3202	7.1090	2.3663
10^{-2}	1.6814	8.9584	2.8076
10^{-1}	4.1571	14.1638	6.1689
1	15.9551	34.7221	72.1526
10^{1}	24.8077	32.4086	28.4549
10^{2}	32.8733	28.8645	22.3299
10^{3}	82.7953	234.8664	22.9091
10^{4}	39.7339	44.6247	118.8180
10^{5}	39.3725	29.1175	113.5092
10^{6}	44.7012	18.7333	105.3424

Table 6: The average MAPE across 15 test slices for each QMap, T1, T2 and PD, against the Equivariant loss hyperparameter, α, for NonLinear Equivariant Imaging (NLEI) with EPI Subsampling.

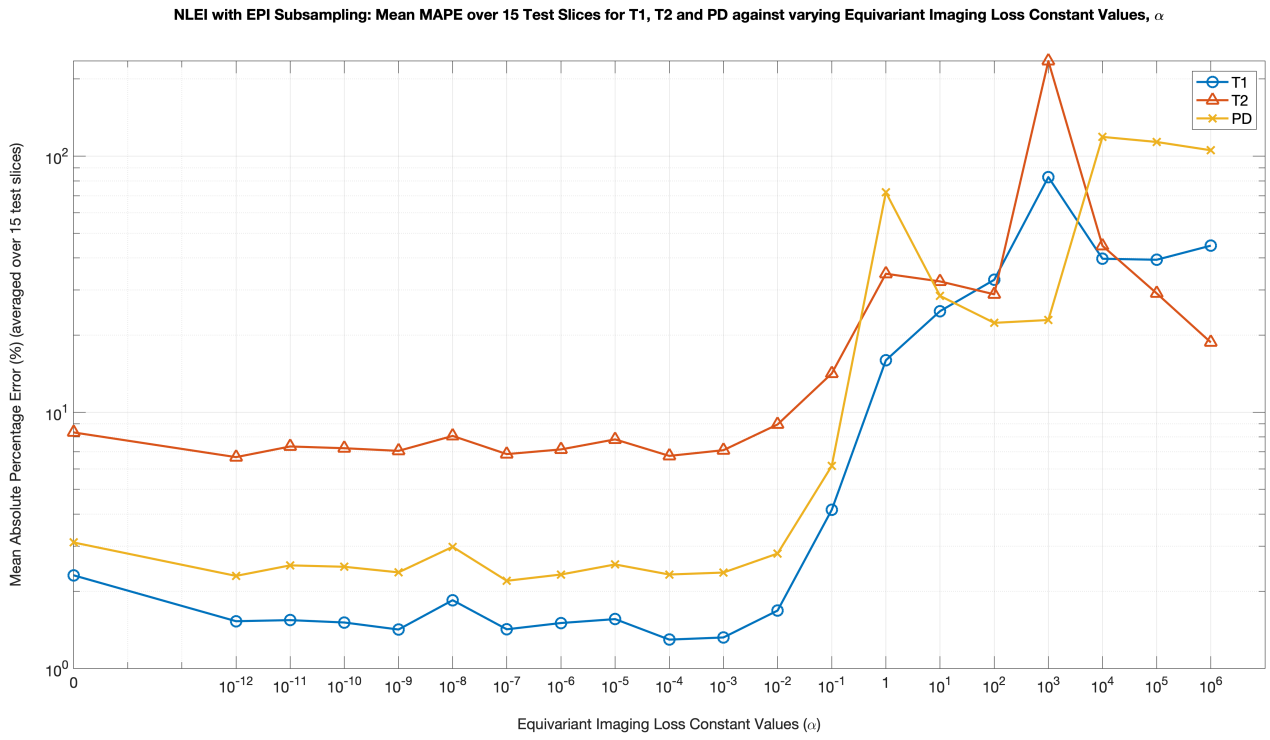


Fig. 6: The graph for the average MAPE across 15 test slices for each QMap, T1, T2 and PD, against the Equivariant loss hyperparameter, α, for NonLinear Equivariant Imaging (NLEI) with EPI Subsampling.

NLEI with EPI Subsampling - Mean PSNR			
α	T1 PSNR (dB)	T2 PSNR (dB)	PSNR (dB)
0	36.9056	35.4542	35.8991
10^{-12}	38.9810	37.1024	38.3585
10^{-11}	38.2721	36.3653	37.3931
10^{-10}	38.3038	35.9135	37.8005
10^{-9}	39.0430	37.0306	37.7414
10^{-8}	37.8366	36.2374	36.0738
10^{-7}	39.0094	37.0378	38.4272
10^{-6}	37.3860	36.6901	38.1582
10^{-5}	37.7602	36.0914	37.4961
10^{-4}	39.2725	37.0679	38.2944
10^{-3}	39.0171	37.5050	38.2829
10^{-2}	38.0982	35.9291	36.4459
10^{-1}	33.4653	35.5957	30.4087
1	21.2098	29.3584	10.6199
10^{1}	19.1448	29.7561	17.5979
10^{2}	17.6816	30.1725	18.9534
10^{3}	11.6431	19.5159	18.8848
10^{4}	16.6225	28.8932	6.7564
10^{5}	16.6768	30.0111	7.1636
10^{6}	15.9038	30.8007	8.0054

Table 7: The average PSNR across 15 test slices for each QMap, T1, T2 and PD, against the Equivariant loss hyperparameter, α, for NonLinear Equivariant Imaging (NLEI) with EPI Subsampling.

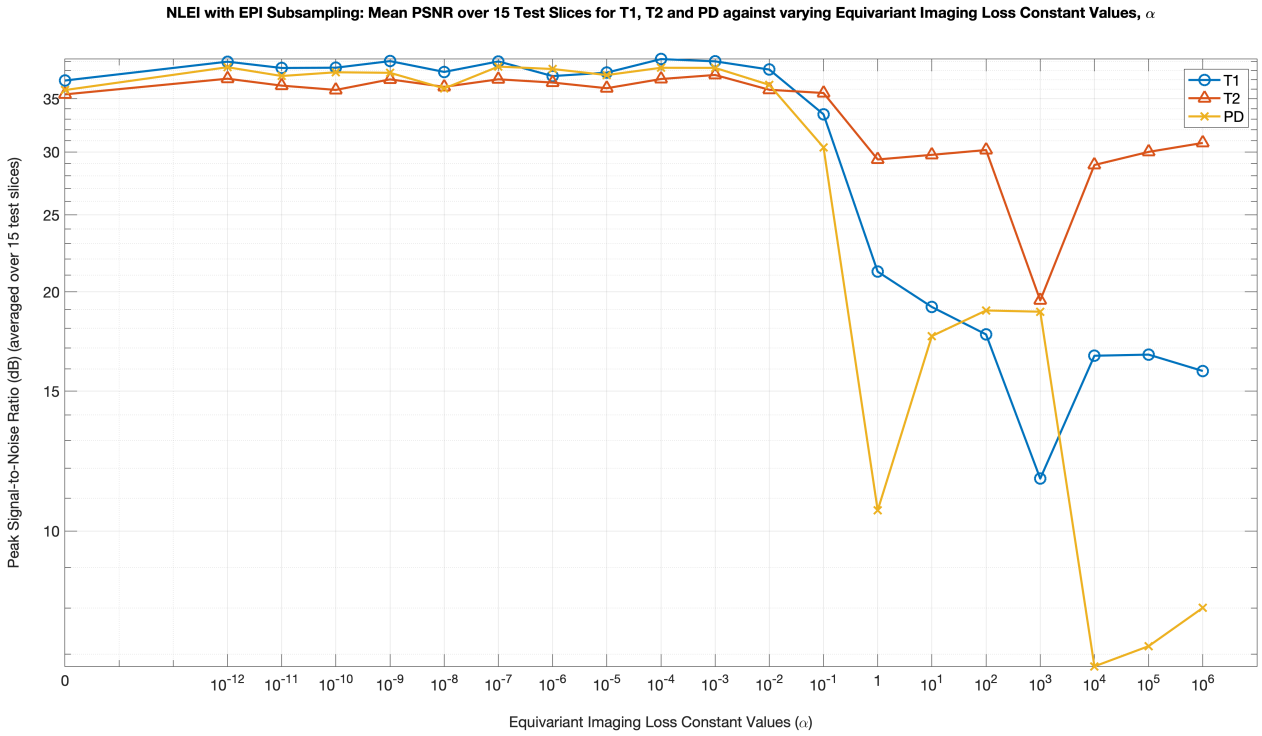


Fig. 7: The graph for the average PSNR across 15 test slices for each QMap, T1, T2 and PD, against the Equivariant loss hyperparameter, α, for NonLinear Equivariant Imaging (NLEI) with EPI Subsampling.

NLEI with EPI Subsampling - Mean SSIM			
α	T1 SSIM	T2 SSIM	PD SSIM
0	0.9843	0.9478	0.9732
10^{-12}	0.9894	0.9646	0.9844
10^{-11}	0.9876	0.9573	0.9821
10^{-10}	0.9875	0.9544	0.9820
10^{-9}	0.9888	0.9636	0.9826
10^{-8}	0.9858	0.9552	0.9735
10^{-7}	0.9894	0.9640	0.9834
10^{-6}	0.9869	0.9614	0.9826
10^{-5}	0.9872	0.9555	0.9812
10^{-4}	0.9898	0.9642	0.9837
10^{-3}	0.9898	0.9660	0.9836
10^{-2}	0.9877	0.9540	0.9744
10^{-1}	0.9499	0.9443	0.9126
1	0.7553	0.6870	0.6761
10^{1}	0.6820	0.7155	0.6599
10^{2}	0.5933	0.7536	0.6510
10^{3}	0.4642	0.4123	0.6470
10^{4}	0.5184	0.5524	0.6202
10^{5}	0.5220	0.7527	0.6245
10^{6}	0.4779	0.8412	0.6315

Table 8: The average SSIM across 15 test slices for each QMap, T1, T2 and PD, against the Equivariant loss hyperparameter, α, for NonLinear Equivariant Imaging (NLEI) with EPI Subsampling.

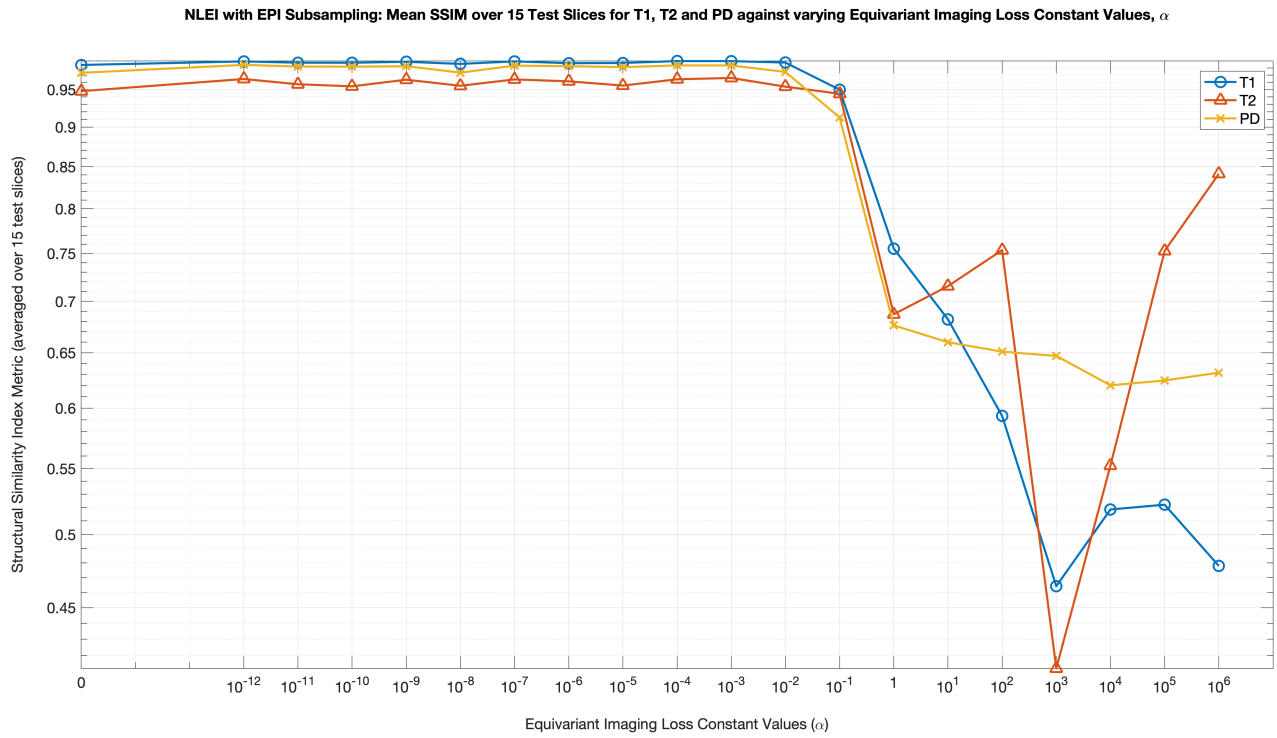


Fig. 8: The graph for the average SSIM across 15 test slices for each QMap, T1, T2 and PD, against the Equivariant loss hyperparameter, α, for NonLinear Equivariant Imaging (NLEI) with EPI Subsampling.

EI with Spiral Subsampling - Mean MAE			
α	T1 MAE (s)	T2 MAE (s)	PD MAE (a.u)
0	0.0538	0.0164	0.0147
10^{-12}	0.0521	0.0159	0.0166
10^{-11}	0.0535	0.0161	0.0162
10^{-10}	0.0545	0.0163	0.0163
10^{-9}	0.0523	0.0159	0.0174
10^{-8}	0.0563	0.0178	0.0229
10^{-7}	0.0540	0.0167	0.0177
10^{-6}	0.0533	0.0163	0.0153
10^{-5}	0.0506	0.0157	0.0135
10^{-4}	0.0525	0.0163	0.0171
10^{-3}	0.0518	0.0158	0.0146
10^{-2}	0.0530	0.0164	0.0153
10^{-1}	0.0543	0.0165	0.0223
1	0.0601	0.0192	0.0231
10^{1}	0.0734	0.0209	0.0499
10^{2}	0.1451	0.0315	0.1849
10^{3}	0.1767	0.0315	0.1737
10^{4}	0.1777	0.0310	0.1050
10^{5}	0.1798	0.0305	0.2523
10^{6}	0.1799	0.0305	0.2931

Table 9: The average MAE across 15 test slices for each QMap, T1, T2 and PD, against the Equivariant loss hyperparameter, α, for linear Equivariant Imaging (EI) with Spiral Subsampling.

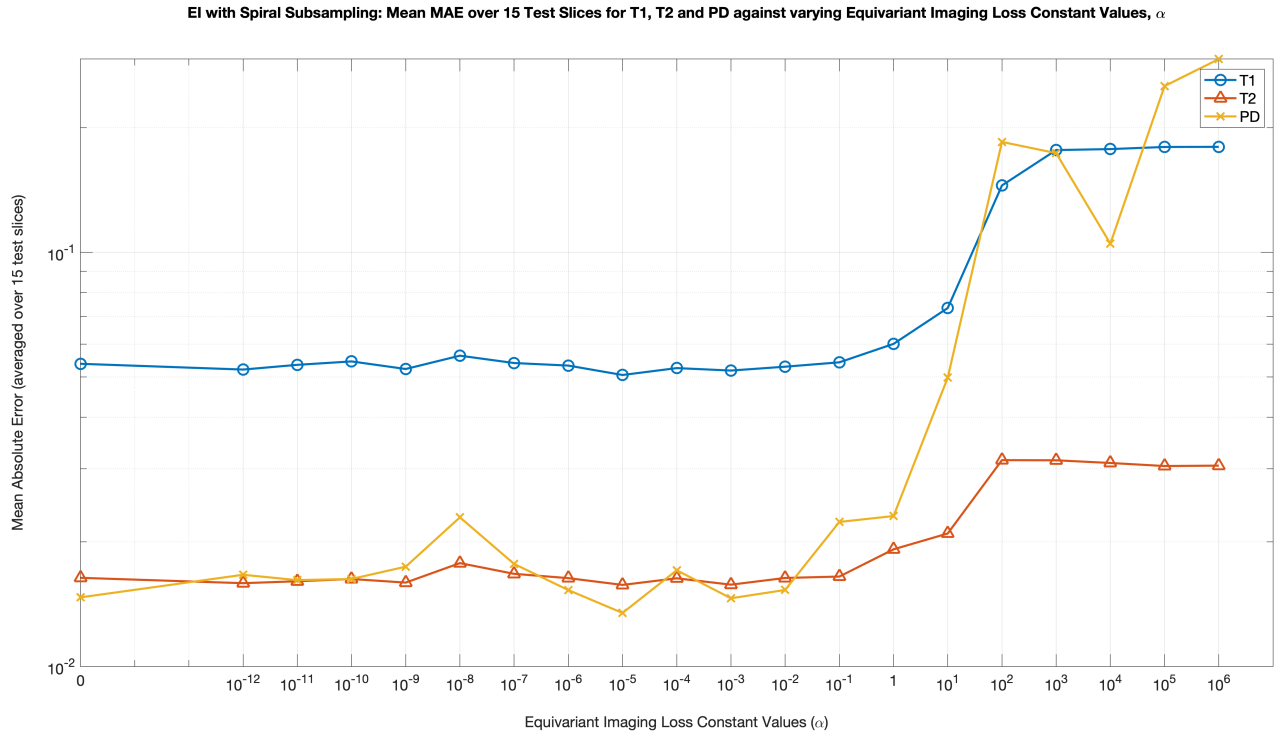


Fig. 9: The graph for the average MAE across 15 test slices for each QMap, T1, T2 and PD, against the Equivariant loss hyperparameter, α, for linear Equivariant Imaging (EI) with Spiral Subsampling.

EI with Spiral Subsampling - Mean MAPE			
α	T1 MAPE (%)	T2 MAPE (%)	PD MAPE (%)
0	4.2072	8.7901	5.6714
10^{-12}	4.0780	8.6528	6.4161
10^{-11}	4.1792	8.8209	6.2615
10^{-10}	4.3127	9.1114	6.1888
10^{-9}	4.1027	8.5670	6.7515
10^{-8}	4.4946	9.7638	8.6750
10^{-7}	4.2808	8.9900	6.9081
10^{-6}	4.2826	8.7033	5.8529
10^{-5}	4.0897	8.4305	5.2789
10^{-4}	4.1112	8.4252	6.5966
10^{-3}	4.0683	8.6273	5.6712
10^{-2}	4.1309	8.7967	5.9373
10^{-1}	4.2045	8.9071	8.5592
1	4.7045	10.4998	8.8462
10^{1}	5.6234	10.2978	19.2170
10^{2}	11.1458	16.9386	72.8756
10^{3}	14.3074	15.6273	67.6573
10^{4}	15.0264	16.9562	41.6878
10^{5}	15.6406	14.4145	101.4867
10^{6}	15.6578	14.6547	117.4045

Table 10: The average MAPE across 15 test slices for each QMap, T1, T2 and PD, against the Equivariant loss hyperparameter, α, for linear Equivariant Imaging (EI) with Spiral Subsampling.

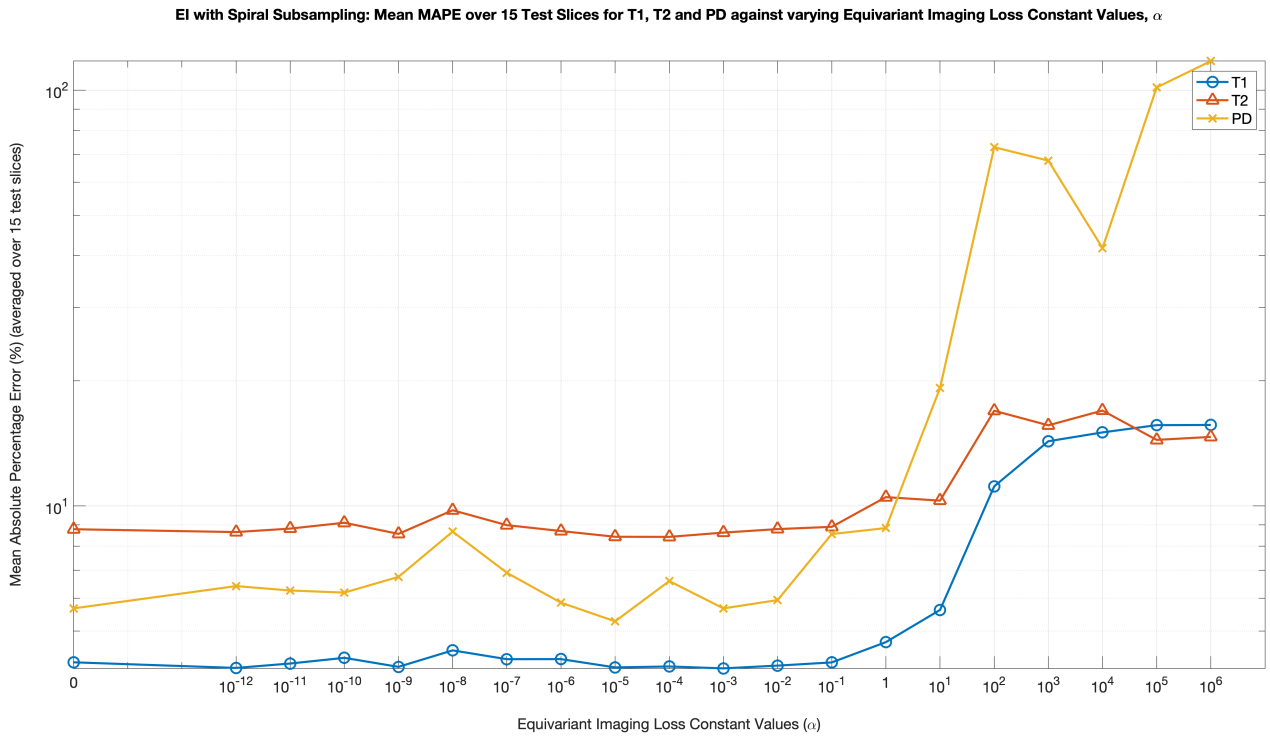


Fig. 10: The graph for the average MAPE across 15 test slices for each QMap, T1, T2 and PD, against the Equivariant loss hyperparameter, α, for linear Equivariant Imaging (EI) with Spiral Subsampling.

EI with Spiral Subsampling - Mean PSNR				
α	T1 PSNR (dB)	T2 PSNR (dB)	PD PSNR (dB)	TSMI PSNR (dB)
0	33.0338	36.1964	30.7113	18.8197
10^{-12}	33.3766	36.8253	30.0492	21.0106
10^{-11}	32.9535	36.3929	30.2479	21.4194
10^{-10}	32.7302	36.4768	30.0981	21.3871
10^{-9}	33.3861	36.5719	29.7736	21.5697
10^{-8}	32.3717	35.4812	27.2573	18.6427
10^{-7}	32.7760	36.0602	29.6220	21.4802
10^{-6}	33.2046	36.2564	30.5388	21.3567
10^{-5}	33.5820	36.7728	31.4401	21.3110
10^{-4}	33.2867	36.3890	29.8238	21.7094
10^{-3}	33.5632	36.7695	30.9022	21.9795
10^{-2}	33.1167	36.2874	30.5400	21.5254
10^{-1}	32.9669	36.4769	27.9505	21.8362
1	31.5910	33.8421	27.6364	19.2568
10^{1}	30.7331	34.4141	21.5620	21.8899
10^{2}	25.2856	31.7330	10.3843	17.8771
10^{3}	23.8945	31.6696	10.2516	17.3663
10^{4}	24.0135	31.8874	14.2755	19.1679
10^{5}	24.0452	31.7073	8.1859	20.0274
10^{6}	24.0428	31.7152	6.8634	19.9352

Table 11: The average PSNR across 15 test slices for each QMap, T1, T2 and PD, against the Equivariant loss hyperparameter, α, for linear Equivariant Imaging (EI) with Spiral Subsampling.

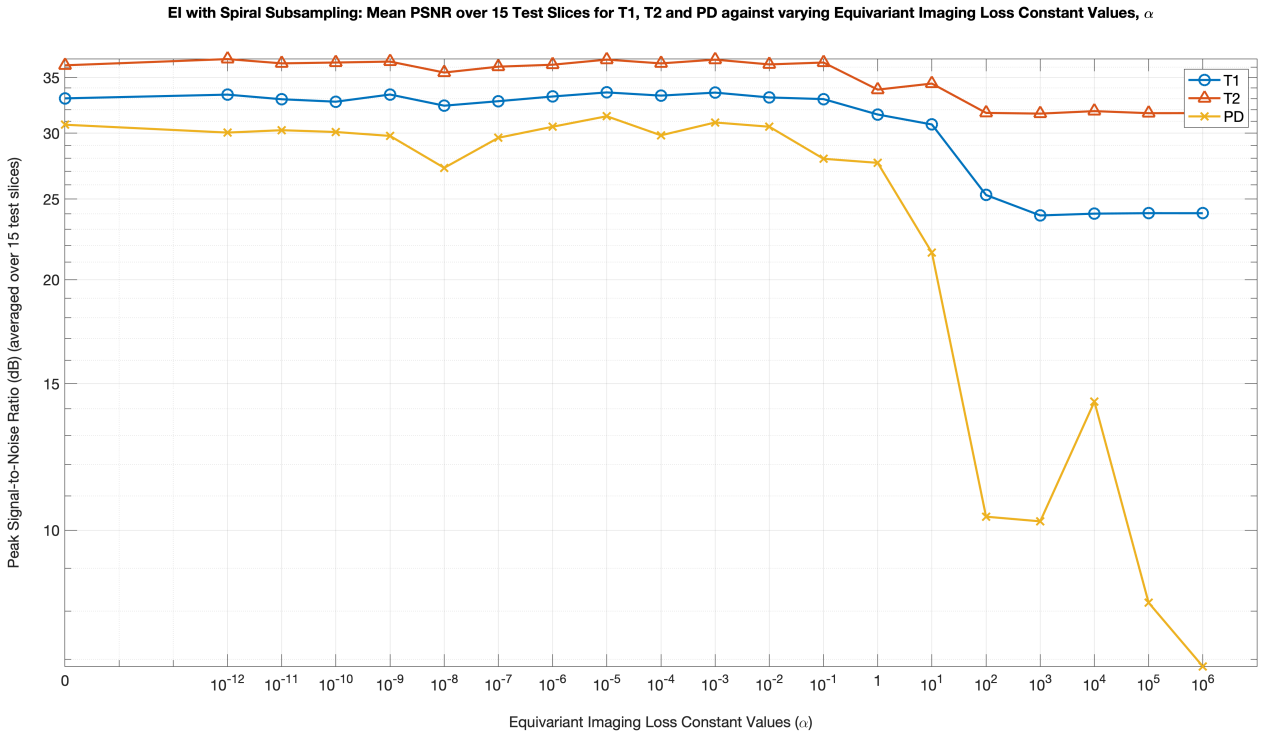


Fig. 11: The graph for the average PSNR across 15 test slices for each QMap, T1, T2 and PD, against the Equivariant loss hyperparameter, α, for linear Equivariant Imaging (EI) with Spiral Subsampling.

EI with Spiral Subsampling - Mean SSIM				
α	T1 SSIM	T2 SSIM	PD SSIM	TSMI SSIM
0	0.9392	0.9490	0.8872	0.6596
10^{-12}	0.9432	0.9530	0.8927	0.6612
10^{-11}	0.9407	0.9515	0.8909	0.6605
10^{-10}	0.9378	0.9513	0.8884	0.6596
10^{-9}	0.9429	0.9520	0.8940	0.6619
10^{-8}	0.9364	0.9429	0.8783	0.6555
10^{-7}	0.9392	0.9486	0.8891	0.6622
10^{-6}	0.9412	0.9503	0.8922	0.6588
10^{-5}	0.9464	0.9530	0.8969	0.6581
10^{-4}	0.9416	0.9496	0.8912	0.6652
10^{-3}	0.9439	0.9534	0.8941	0.6680
10^{-2}	0.9407	0.9494	0.8928	0.6613
10^{-1}	0.9392	0.9502	0.8855	0.6676
1	0.9261	0.9358	0.8757	0.6718
10^{1}	0.8948	0.9235	0.8502	0.6732
10^{2}	0.7862	0.8817	0.7137	0.6492
10^{3}	0.7649	0.8809	0.7085	0.6392
10^{4}	0.7650	0.8860	0.7543	0.6373
10^{5}	0.7639	0.8857	0.6392	0.6186
10^{6}	0.7638	0.8855	0.6216	0.6151

Table 12: The average SSIM across 15 test slices for each QMap, T1, T2 and PD, against the Equivariant loss hyperparameter, α, for linear Equivariant Imaging (EI) with Spiral Subsampling.

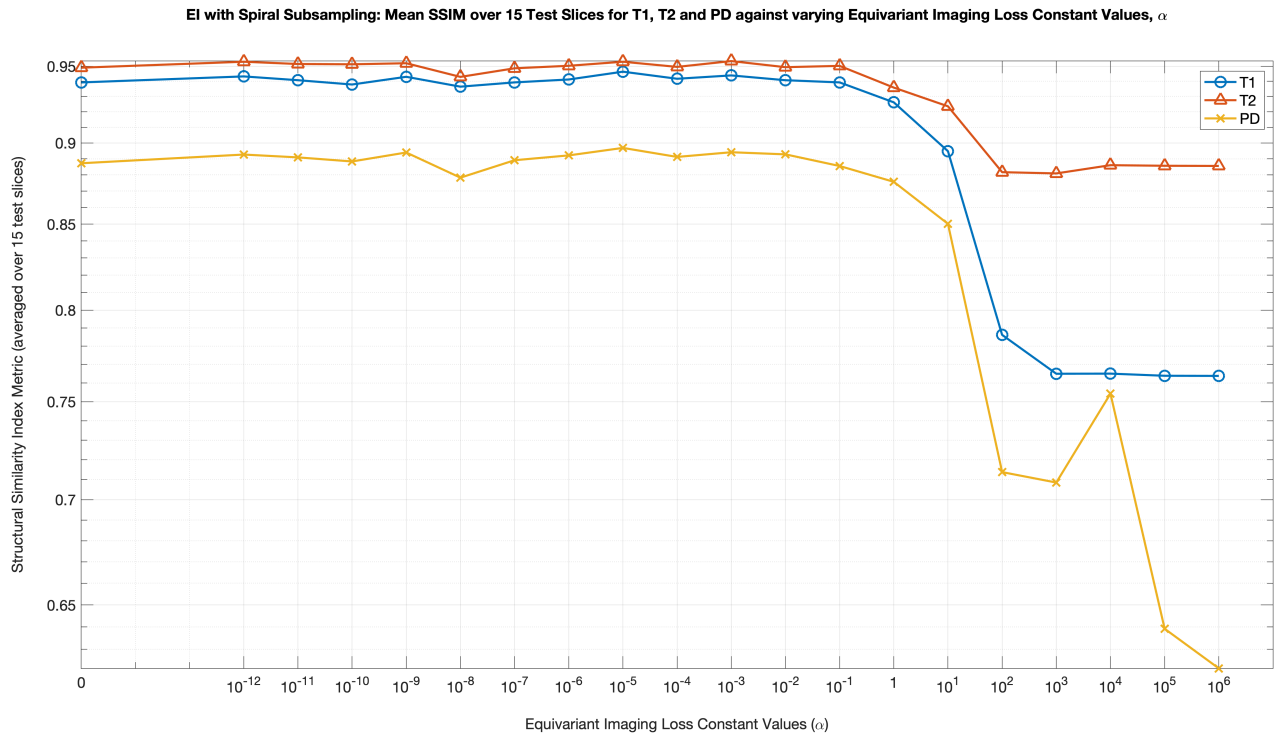


Fig. 12: The graph for the average SSIM across 15 test slices for each QMap, T1, T2 and PD, against the Equivariant loss hyperparameter, α, for linear Equivariant Imaging (EI) with Spiral Subsampling.

EI with EPI Subsampling - Mean MAE			
α	T1 MAE (s)	T2 MAE (s)	PD MAE (a.u)
0	0.3375	0.1650	0.0774
10^{-12}	0.3554	0.0831	0.0756
10^{-11}	0.2395	0.0967	0.0718
10^{-10}	0.2732	0.0882	0.0917
10^{-9}	0.2022	0.0674	0.0886
10^{-8}	0.1943	0.2332	0.0731
10^{-7}	0.1964	0.1814	0.0381
10^{-6}	0.2449	0.2249	0.0279
10^{-5}	0.1675	0.2048	0.0348
10^{-4}	0.2449	0.0815	0.0498
10^{-3}	0.2806	0.0931	0.0457
10^{-2}	0.1096	0.0451	0.0268
10^{-1}	0.0844	0.2055	0.0142
1	0.0950	0.0478	0.0365
10^{1}	0.1194	0.1795	0.1412
10^{2}	0.4487	0.3139	0.1347
10^{3}	1.4173	0.0372	0.1722
10^{4}	0.1861	0.4790	0.2943
10^{5}	0.1949	0.5075	0.2959
10^{6}	0.3137	0.0589	0.2968

Table 13: The average MAE across 15 test slices for each QMap, T1, T2 and PD, against the Equivariant loss hyperparameter, α, for linear Equivariant Imaging (EI) with EPI Subsampling.

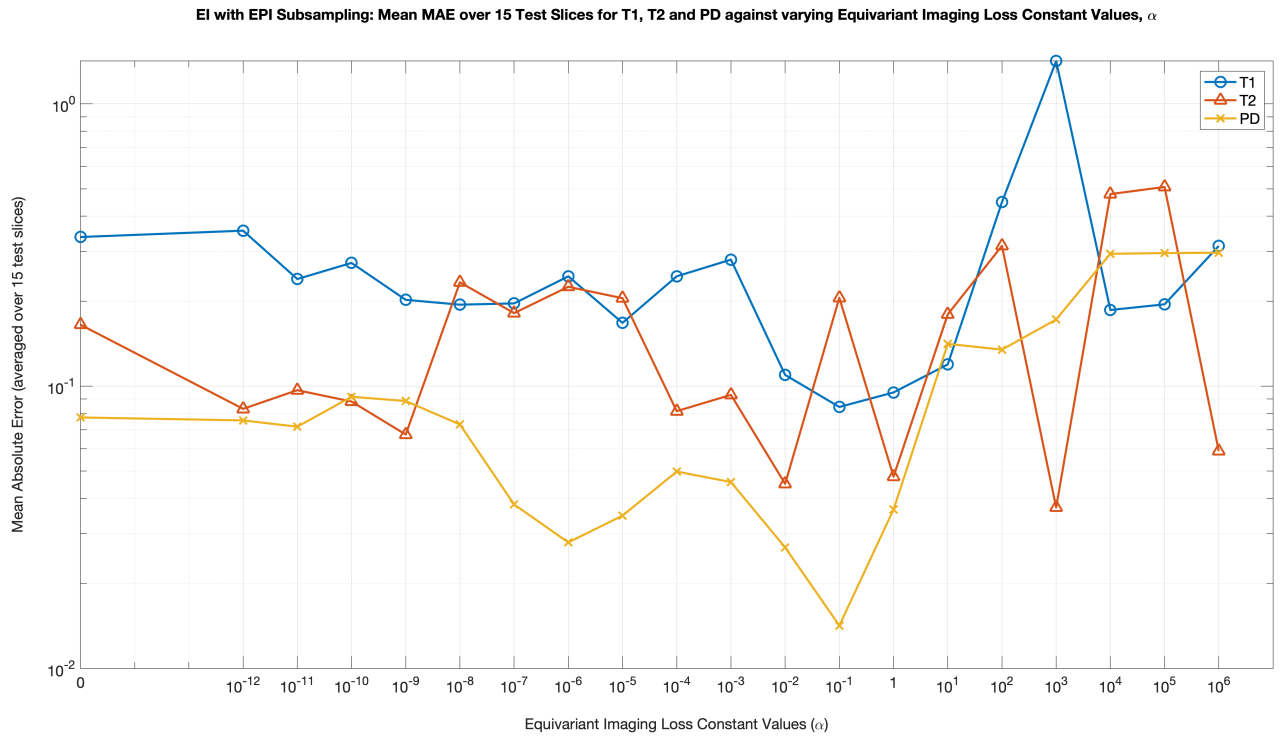


Fig. 13: The graph for the average MAE across 15 test slices for each QMap, T1, T2 and PD, against the Equivariant loss hyperparameter, α, for linear Equivariant Imaging (EI) with EPI Subsampling.

EI with EPI Subsampling - Mean MAPE			
α	T1 MAPE (%)	T2 MAPE (%)	PD MAPE (%)
0	26.3318	135.5899	27.7157
10^{-12}	26.1461	74.1114	26.7611
10^{-11}	18.2042	99.2322	27.3531
10^{-10}	19.0999	67.3423	36.7881
10^{-9}	14.3593	50.3731	31.6792
10^{-8}	15.3900	177.1664	27.2429
10^{-7}	13.2067	173.7378	13.1139
10^{-6}	17.3777	183.5313	10.1765
10^{-5}	11.5588	148.5074	13.4065
10^{-4}	16.2921	69.1706	19.4256
10^{-3}	20.7409	70.8022	17.7070
10^{-2}	7.4711	33.5549	10.6282
10^{-1}	6.0060	191.1255	5.4268
1	8.7539	37.2691	14.7984
10^{1}	9.6941	142.8419	56.2033
10^{2}	37.9268	309.2443	53.9230
10^{3}	141.3228	22.9724	71.1500
10^{4}	16.9006	485.8691	117.8429
10^{5}	18.3943	513.8505	118.4888
10^{6}	33.1389	37.1800	118.8190

Table 14: The average MAPE across 15 test slices for each QMap, T1, T2 and PD, against the Equivariant loss hyperparameter, α, for linear Equivariant Imaging (EI) with EPI Subsampling.

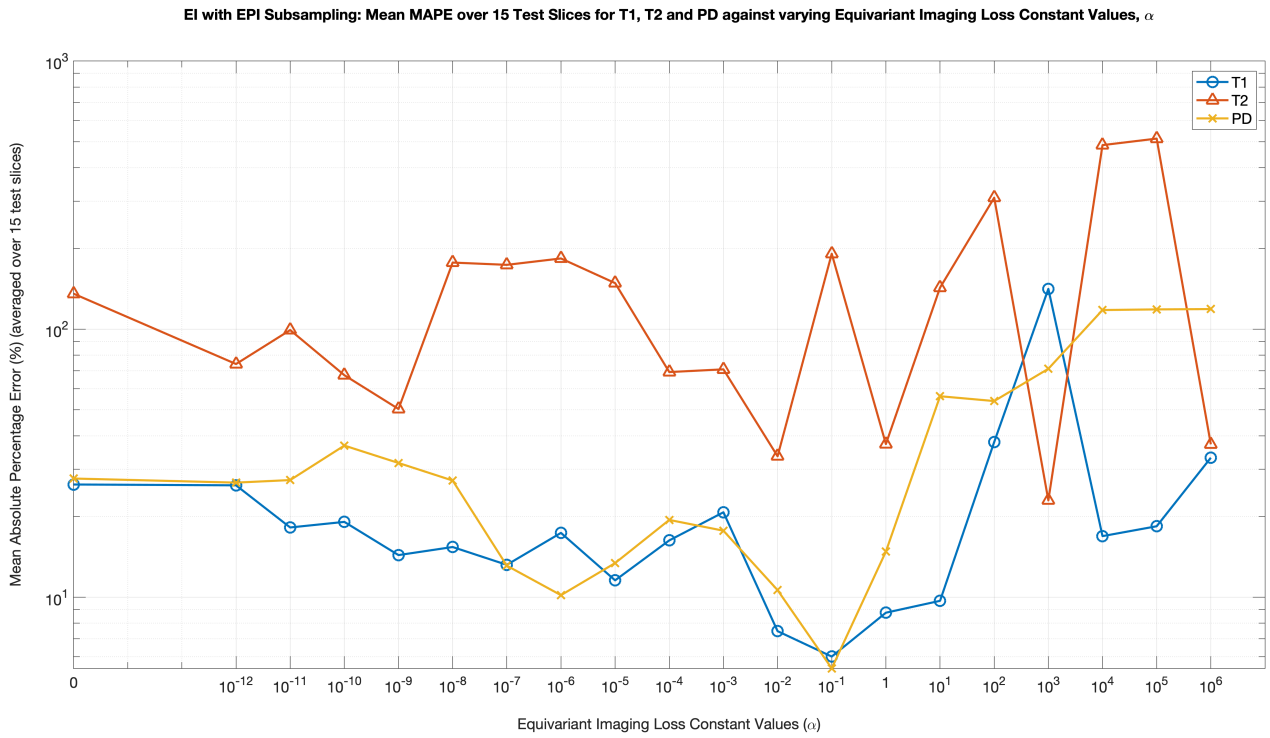


Fig. 14: The graph for the average MAPE across 15 test slices for each QMap, T1, T2 and PD, against the Equivariant loss hyperparameter, α, for linear Equivariant Imaging (EI) with EPI Subsampling.

EI with EPI Subsampling - Mean PSNR				
α	T1 PSNR (dB)	T2 PSNR (dB)	PD PSNR (dB)	TSMI PSNR (dB)
0	18.2728	20.7138	17.8021	0.3392
10^{-12}	17.6452	24.0347	18.0257	0.4167
10^{-11}	18.9077	27.0630	19.4534	-5.1060
10^{-10}	19.5507	23.1897	15.6966	0.6164
10^{-9}	19.6810	22.6231	16.7673	1.6752
10^{-8}	21.6021	17.4648	18.9366	-2.7664
10^{-7}	20.4500	20.7188	23.2824	2.5408
10^{-6}	20.5135	18.2230	25.0303	3.9077
10^{-5}	23.3167	18.1354	22.9783	3.3348
10^{-4}	19.7696	26.0009	20.6255	2.8656
10^{-3}	19.8411	23.8267	21.4395	0.6290
10^{-2}	23.3885	31.1333	25.9406	3.2324
10^{-1}	28.6166	20.2872	30.3307	0.5505
1	25.4382	24.6760	23.7842	1.5944
10^{1}	25.2234	19.1101	12.6983	1.4202
10^{2}	13.9856	15.7975	12.8303	2.6748
10^{3}	7.5946	31.4068	11.0399	3.1600
10^{4}	24.0091	14.5836	6.8287	3.3823
10^{5}	23.8720	14.0852	6.7803	-0.4833
10^{6}	20.8934	29.4065	6.7557	-10.1756

Table 15: The average PSNR across 15 test slices for each QMap, T1, T2 and PD, against the Equivariant loss hyperparameter, α, for linear Equivariant Imaging (EI) with EPI Subsampling.

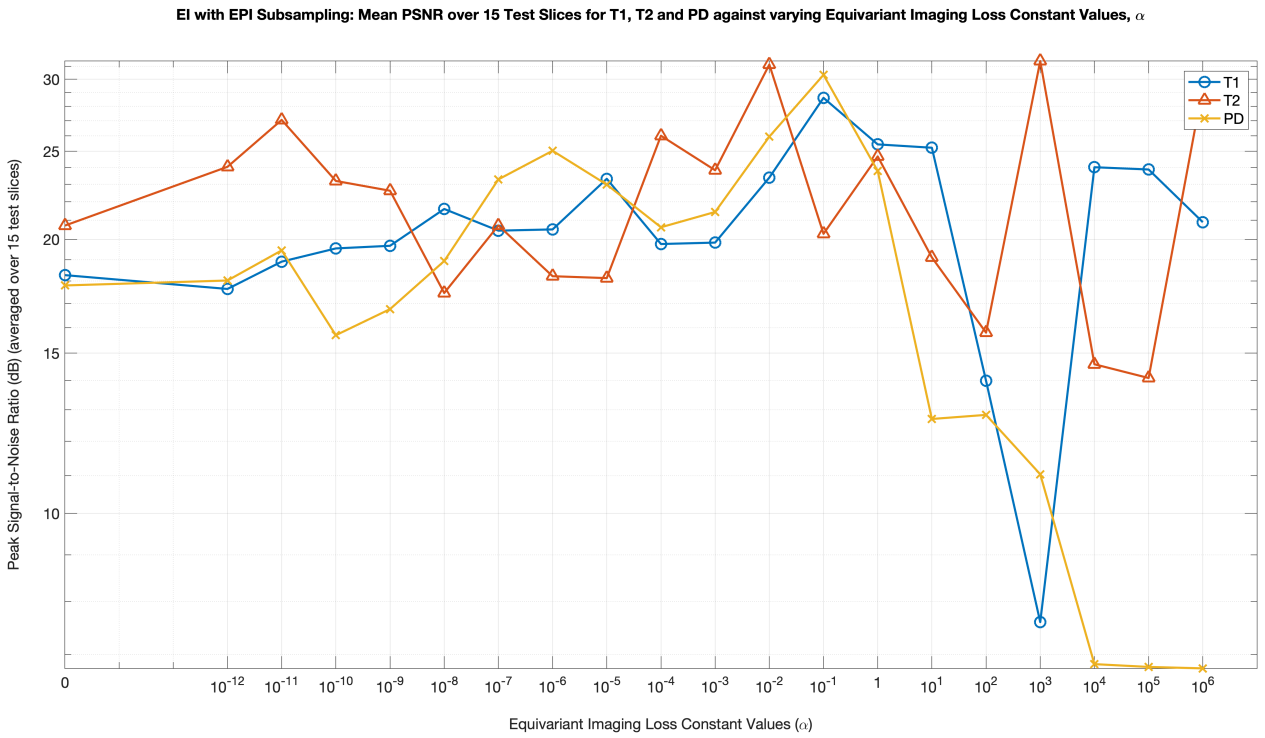


Fig. 15: The graph for the average PSNR across 15 test slices for each QMap, T1, T2 and PD, against the Equivariant loss hyperparameter, α, for linear Equivariant Imaging (EI) with EPI Subsampling.

EI with EPI Subsampling - Mean SSIM				
α	T1 SSIM	T2 SSIM	PD SSIM	TSMI SSIM
0	0.7302	0.6198	0.7043	0.5373
10^{-12}	0.7340	0.6823	0.6956	0.5318
10^{-11}	0.8383	0.7493	0.6976	0.5364
10^{-10}	0.8076	0.6608	0.6787	0.5368
10^{-9}	0.8574	0.8093	0.6377	0.5501
10^{-8}	0.8859	0.6241	0.6601	0.5373
10^{-7}	0.8545	0.6615	0.8607	0.5437
10^{-6}	0.8368	0.6112	0.8329	0.5493
10^{-5}	0.9020	0.6766	0.8084	0.5519
10^{-4}	0.8425	0.7162	0.7690	0.5457
10^{-3}	0.8066	0.7049	0.7367	0.5424
10^{-2}	0.9230	0.8376	0.9050	0.5542
10^{-1}	0.9521	0.6520	0.9507	0.5421
1	0.9194	0.8535	0.8451	0.5499
10^{1}	0.8714	0.6989	0.6805	0.5530
10^{2}	0.6772	0.5798	0.7001	0.5542
10^{3}	0.5863	0.8663	0.6865	0.5486
10^{4}	0.7612	0.5542	0.6212	0.5634
10^{5}	0.7580	0.5501	0.6205	0.5453
10^{6}	0.7258	0.6540	0.6202	0.5075

Table 16: The average SSIM across 15 test slices for each QMap, T1, T2 and PD, against the Equivariant loss hyperparameter, α, for linear Equivariant Imaging (EI) with EPI Subsampling.

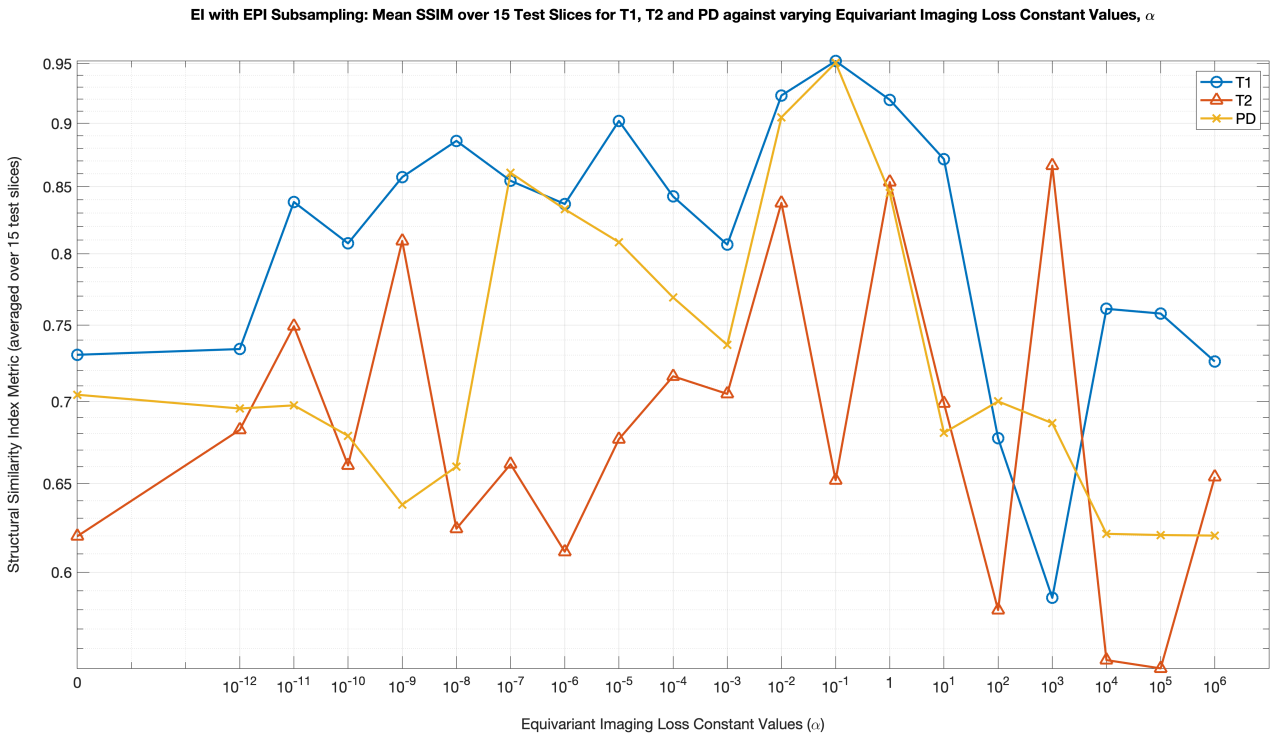


Fig. 16: The graph for the average SSIM across 15 test slices for each QMap, T1, T2 and PD, against the Equivariant loss hyperparameter, α, for linear Equivariant Imaging (EI) with EPI Subsampling.

NLEI with Spiral Subsampling - Mean QMaps				
α	MAE (s)	MAPE (%)	PSNR (dB)	SSIM
0	0.4328	404.7980	12.3972	0.8853
10^{-12}	0.0386	9.5690	30.7360	0.9099
10^{-11}	0.0350	8.5966	31.6014	0.9168
10^{-10}	0.0287	6.2665	33.5922	0.9274
10^{-9}	0.0286	6.4052	33.5261	0.9282
10^{-8}	**0.0274**	**5.9153**	**33.9631**	**0.9292**
10^{-7}	0.0290	6.4024	33.3679	0.9260
10^{-6}	0.0287	6.5446	33.1167	0.9260
10^{-5}	0.0303	7.3664	32.5804	0.9271
10^{-4}	0.0309	7.1517	32.7060	0.9233
10^{-3}	0.0288	6.4026	33.4722	0.9261
10^{-2}	0.0327	7.1470	32.4181	0.9187
10^{-1}	0.0369	7.9833	31.6051	0.9046
1	0.0681	17.8357	26.6043	0.8576
10^{1}	0.1173	32.5374	22.7236	0.7946
10^{2}	0.1343	37.6572	21.8036	0.7827
10^{3}	0.1117	36.9561	22.5175	0.7833
10^{4}	0.3141	42.2402	19.9919	0.6199
10^{5}	0.2620	73.8749	17.5986	0.5108
10^{6}	0.2546	46.6075	19.4733	0.5901

Table 17: The average result using all QMaps, T1, T2 and PD, (for 15 test slices) with respect to a particular metric against varying the Equivariant loss hyperparameter, α, for NonLinear Equivariant Imaging (NLEI) with Spiral Subsampling.

EI with Spiral Subsampling - Mean QMaps				
α	MAE (s)	MAPE (%)	PSNR (dB)	SSIM
0	0.0283	6.2229	33.3138	0.9252
10^{-12}	0.0282	6.3823	33.4170	0.9296
10^{-11}	0.0286	6.4206	33.1981	0.9277
10^{-10}	0.0290	6.5376	33.1017	0.9258
10^{-9}	0.0285	6.4737	33.2439	0.9296
10^{-8}	0.0323	7.6445	31.7034	0.9192
10^{-7}	0.0295	6.7263	32.8194	0.9257
10^{-6}	0.0283	6.2796	33.3333	0.9279
10^{-5}	**0.0266**	**5.9331**	**33.9316**	**0.9321**
10^{-4}	0.0286	6.3777	33.1665	0.9275
10^{-3}	0.0274	6.1223	33.7450	0.9305
10^{-2}	0.0282	6.2883	33.3147	0.9276
10^{-1}	0.0310	7.2236	32.4648	0.9250
1	0.0341	8.0168	31.0232	0.9125
10^{1}	0.0481	11.7127	28.9031	0.8895
10^{2}	0.1205	33.6533	22.4676	0.7939
10^{3}	0.1273	32.5307	21.9385	0.7848
10^{4}	0.1046	24.5568	23.3921	0.8018
10^{5}	0.1542	43.8473	21.3128	0.7629
10^{6}	0.1679	49.2390	20.8738	0.7570

Table 19: The average result using all QMaps, T1, T2 and PD, (for 15 test slices) with respect to a particular metric against varying the Equivariant loss hyperparameter, α, for linear Equivariant Imaging (EI) with Spiral Subsampling.

NLEI with EPI Subsampling - Mean QMaps				
α	MAE (s)	MAPE (%)	PSNR (dB)	SSIM
0	0.0189	4.5833	36.0863	0.9685
10^{-12}	0.0136	3.5007	38.1473	0.9795
10^{-11}	0.0145	3.8056	37.3435	0.9757
10^{-10}	0.0145	3.7459	37.3393	0.9746
10^{-9}	0.0133	3.6179	37.9383	0.9783
10^{-8}	0.0162	4.3028	36.7159	0.9715
10^{-7}	0.0131	3.4936	38.1582	0.9789
10^{-6}	0.0143	3.6619	37.4114	0.9769
10^{-5}	0.0149	3.9790	37.1159	0.9746
10^{-4}	**0.0127**	**3.4579**	38.2116	0.9792
10^{-3}	0.0128	3.5985	**38.2683**	**0.9798**
10^{-2}	0.0156	4.4824	36.8244	0.9720
10^{-1}	0.0293	8.1633	33.1566	0.9356
1	0.1622	40.9433	20.3960	0.7061
10^{1}	0.1588	28.5571	22.1663	0.6858
10^{2}	0.1826	28.0226	22.2691	0.6660
10^{3}	0.4333	113.5236	16.6813	0.5078
10^{4}	0.2921	67.7255	17.4240	0.5637
10^{5}	0.2809	60.6664	17.9505	0.6331
10^{6}	0.2892	56.2590	18.2367	0.6502

Table 18: The average result using all QMaps, T1, T2 and PD, (for 15 test slices) with respect to a particular metric against varying the Equivariant loss hyperparameter, α, for NonLinear Equivariant Imaging (NLEI) with EPI Subsampling.

EI with EPI SubSampling - Mean QMaps				
α	MAE (s)	MAPE (%)	PSNR (dB)	SSIM
0	0.1933	63.2125	18.9296	0.1410
10^{-12}	0.1713	42.3396	19.9019	0.1529
10^{-11}	0.1360	48.2632	21.8081	0.2405
10^{-10}	0.1510	41.0768	19.4790	0.3307
10^{-9}	0.1194	32.1372	19.6905	0.3151
10^{-8}	0.1669	73.2664	19.3345	0.3099
10^{-7}	0.1386	66.6862	21.4837	0.3529
10^{-6}	0.1659	70.3618	21.2556	0.3636
10^{-5}	0.1357	57.8243	21.4768	0.3587
10^{-4}	0.1254	34.9628	22.1320	0.3412
10^{-3}	0.1398	36.4167	21.7024	0.3338
10^{-2}	0.0605	**17.2181**	**26.8208**	**0.4651**
10^{-1}	0.1014	67.5194	26.4115	0.2606
1	**0.0598**	20.2738	24.6328	0.2696
10^{1}	0.1467	69.5798	19.0106	0.1639
10^{2}	0.2991	133.6980	14.2045	0.0843
10^{3}	0.5422	78.4817	16.6804	0.1967
10^{4}	0.3198	206.8709	15.1405	0.0963
10^{5}	0.3328	216.9112	14.9125	0.0946
10^{6}	0.2231	63.0460	19.0185	0.2835

Table 20: The average result using all QMaps, T1, T2 and PD, (for 15 test slices) with respect to a particular metric against varying the Equivariant loss hyperparameter, α, for linear Equivariant Imaging (EI) with EPI Subsampling.